What Causes Anthropogenic Ocean Warming to Emerge from Internal Variability in a Coupled Model?

YONA SILVY,[a] JEAN-BAPTISTE SALLÉE,[a] ERIC GUILYARDI,[a,b] JULIETTE MIGNOT,[a] AND CLÉMENT ROUSSET[a]

[a] *LOCEAN-IPSL, Laboratoire d'Océanographie et du Climat: Expérimentation et Approches Numériques, Sorbonne Université/CNRS/IRD/MNHN, Paris, France*
[b] *NCAS-Climate, University of Reading, Reading, United Kingdom*

(Manuscript received 1 February 2022, in final form 26 July 2022)

ABSTRACT: In response to increasing human emissions, the global ocean is continually warming. The spatial distribution of this warming can result from several mechanisms, difficult to disentangle in observations. Idealized modeling studies have successfully separated the contribution of additional heat passively entering the ocean from the contribution of the changing circulation redistributing the pre-existing heat in response to perturbations in air–sea fluxes. However, the time scales of these different contributions have been largely unexplored so far. Here, we revisit this decomposition with a novel numerical framework to investigate the mechanisms driving regional ocean warming and its emergence from internal variability. Based on the IPSL-CM6A-LR coupled model and its large ensemble of transient climate change simulations, we extract both the internal fluctuations and the externally forced signal in each component of the surface fluxes. With a stand-alone configuration of the ocean, we then test the response to perturbations applied on all surface fluxes together or individually. We find that the contribution of the different processes can largely vary in time, reinforcing or counteracting each other, causing the time of emergence of subsurface temperature changes to be advanced or delayed. Anthropogenic warming in the upper ocean water masses is generally driven by the uptake of excess heat passively stored by the ocean circulation. Circulation changes have a minor role at the time when these signals emerge. On the contrary, in the deeper ocean, circulation changes are much more sensitive to surface forcings and play an important role in setting the time scales of ocean warming, through redistributive warming or cooling.

KEYWORDS: Ocean; Meridional overturning circulation; Coupled models; Ensembles: Numerical analysis/modeling; Climate variability

1. Introduction

Global ocean warming is a key indicator of human-induced climate change, accounting for 91% of the observed energy increase in the climate system between 1971 and 2018 (IPCC 2021). Multidecadal increase in global ocean heat content results from a net global air–sea heat flux into the ocean. Ocean heat content change has, however, not been uniformly distributed over the global ocean, with some regions experiencing rapid heat content increase while others have experienced no change, or a slight decrease in the past 50 years (Fox-Kemper et al. 2021). Processes shaping this regional distribution of heat content change control local ocean temperature change relevant for impacts on ecosystems and societies, and also control time scales at which climate change signals penetrate into the ocean.

Spatial patterns of heat content change are caused by a combination of 1) air–sea heat flux perturbation causing surface temperature anomalies, which are then transported into the ocean interior by the ocean circulation, and 2) changes in ocean circulation redistributing temperature internally in the ocean. Various methodologies have been proposed to decompose temperature change into these two processes, assuming that process 1 is a purely passive process where surface temperature anomalies are advected by the climatological mean circulation and that process 2 is a purely redistributive process where circulation variability transports the climatological mean temperature tracer (Banks and Gregory 2006; Xie and Vallis 2012; Winton et al. 2013; Marshall et al. 2015; Armour et al. 2016; Gregory et al. 2016; Garuba and Klinger 2016; Zanna et al. 2019b; Bronselaer and Zanna 2020). The relative contributions of passive versus redistributive processes on ocean temperature change vary largely with the time scales considered. At decadal time scale, redistribution dominates temperature variability in response to large internally generated variations in the ocean circulation (Zika et al. 2021; Rathore et al. 2020). On longer time scales, as the surface heat flux forcing accumulates in response to climate change, passive storage of heat becomes larger (Bronselaer and Zanna 2020). This is particularly clear in regions of large subduction such as the Southern Ocean and the North Atlantic basins, where passive heat accumulates in ventilated water masses, with some modulation in response to forced ocean circulation change (Piecuch et al. 2017; Zanna et al. 2019b; Bronselaer and Zanna 2020).

At multidecadal time scales in the Southern Ocean, surface heat excess associated with climate change enters the ocean at the southern flank of the Antarctic Circumpolar Current (ACC),

Denotes content that is immediately available upon publication as open access.

Supplemental information related to this paper is available at the Journals Online website: https://doi.org/10.1175/JCLI-D-22-0074.s1.

Corresponding author: Yona Silvy, yona.silvy@locean.ipsl.fr

DOI: 10.1175/JCLI-D-22-0074.1

© 2022 American Meteorological Society. For information regarding reuse of this content and general copyright information, consult the AMS Copyright Policy (www.ametsoc.org/PUBSReuseLicenses).

Brought to you by NOAA Central Library | Unauthenticated | Downloaded 01/23/24 09:28 PM UTC

before being passively transported northward and subducted in the ocean interior along the ventilation pathways of the Subantarctic Mode and Antarctic Intermediate Waters (SAMW and AAIW) (Marshall et al. 2015; Frölicher et al. 2015; Gregory et al. 2016; Armour et al. 2016; Liu et al. 2018; Dias et al. 2020; Couldrey et al. 2021). The redistribution signal is, in comparison, weaker and associated with intensifying and poleward-shifting westerly winds, driving increased northward Ekman transport and consequently increased heat subduction and storage at midlatitudes (Fyfe et al. 2007; Liu et al. 2018; Shi et al. 2020).

In contrast, the North Atlantic basin is associated with a larger redistribution signal, even at long time scales, due to a slowdown in the Atlantic meridional overturning circulation (AMOC), which itself is initially largely caused by a reduced air–sea heat loss (resulting in a positive heat flux anomaly) (Mikolajewicz and Voss 2000; Gregory et al. 2016; Garuba and Klinger 2018; Todd et al. 2020). The slowdown of the AMOC weakens the poleward heat transport, causing a redistributive cooling in the subpolar North Atlantic. In the context of coupled models with a prescribed heat flux perturbation, this redistributive cooling feeds back on the surface heat flux and increases the initial heat uptake by the ocean, which further weakens the AMOC, creating a positive loop clearly identified in these specific simulations (Gregory et al. 2016; Todd et al. 2020). In parallel to this redistributive cooling, positive heat flux perturbation causes heat to passively accumulate and to be transferred at depth by deep convection in the subpolar North Atlantic (Xie and Vallis 2012; Winton et al. 2013; Marshall et al. 2015; Gregory et al. 2016; Garuba and Klinger 2016, 2018; Bronselaer and Zanna 2020; Todd et al. 2020; Dias et al. 2020; Williams et al. 2021; Couldrey et al. 2021).

Most studies that investigated temperature change in the framework of passive versus redistribution have focused on the long-term multidecadal response to idealized forcings. For instance, to isolate the passive and redistributive components, Banks and Gregory (2006), Xie and Vallis (2012), Marshall et al. (2015), Armour et al. (2016), Gregory et al. (2016), Garuba and Klinger (2016, 2018), Todd et al. (2020), Dias et al. (2020), and Couldrey et al. (2021) have investigated the century-scale response of the ocean by introducing passive temperature tracers in idealized climate change experiments where CO_2 forcing is instantly doubled or quadrupled, or where CO_2 forcing grows at 1% or 2% per year. Others have compared the century-scale response of the ocean in experiments in which currents are fixed to climatological values to experiments where currents evolve freely under a 1% CO_2 per year scenario (Winton et al. 2013; Bronselaer and Zanna 2020). One study proposed a reconstruction of passive heat storage from a representation of climatological transport processes passively advecting observed SST anomalies (Zanna et al. 2019b). Another reconstructed the passive component of temperature change in observations of the twentieth century and model projections, using the relation diagnosed between anthropogenic carbon and passive heat in idealized simulations and applying it to observations of anthropogenic carbon (Bronselaer and Zanna 2020). Another decomposition that has been proposed on the long-term response to radiative forcing scenarios aimed to trace total changes in temperature to separate contributions from individual air–sea flux perturbations: changes in the surface heat flux, freshwater flux, and wind stress, which can all cause circulation changes and consequently redistribution (Mikolajewicz and Voss 2000; Fyfe et al. 2007; Armour et al. 2016; Gregory et al. 2016; Liu et al. 2018; Garuba and Klinger 2018; Shi et al. 2020; Todd et al. 2020; Dias et al. 2020; Couldrey et al. 2021).

Today, it remains unclear how these passive/redistributive processes and their relative time scales compete with each other and with internal variability in the transient response to realistic historical forcings (CO_2 and other forcings) and the twenty-first-century scenario. In this study, we are interested not only in what processes cause heat storage at the end of the twenty-first century (i.e., the long-term response) but also which processes cause temperature changes to emerge from local internal variability in the ocean interior, which can occur much earlier than 2100 in climate models (Silvy et al. 2020). We will use the notion of the time of emergence (ToE) of climate signals (e.g., Hawkins and Sutton 2012), that is, the time when a signal (e.g., a temperature change) last exceeds and remains above a significance threshold representing the internal variability noise envelope, and apply this notion to ocean interior changes.

We will explore whether the emergence of the subsurface temperature anomalies relies on the rate of increased surface heat flux modulated by the time scales of the unperturbed ocean circulation or on circulation changes themselves, which can fundamentally change the way water masses are ventilated in some regions and reorganize the temperature distribution. The influence of circulation changes acting on the transport of excess heat into the ocean will also be explored, with a nonnegligible role found in some regions and on different time scales.

We investigate the mechanisms of ocean heat storage and their time scales in response to increasing anthropogenic forcings in the framework of the coupled model IPSL-CM6A-LR large ensemble of historical simulations and the Shared Socioeconomic Pathway "ssp245" scenario. In section 2 we present the ensemble and its long-term changes in temperature and ocean heat content with their emergence from internal variability. In section 3 we introduce a modeling framework designed to decompose these changes with a set of sensitivity experiments with an ocean-only model, which is fully described in a companion paper (Silvy et al. 2022). We present the results of these experiments, with a focus on the long-term changes in section 4, confirming the validity of our results with past studies, and investigate the more regional and temporal aspects in section 5 focusing on a few important ventilation pathways. The approach and the general results of this study are finally summarized and discussed in section 6.

2. Long-term changes in the IPSL-CM6A-LR large ensemble

a. *Model and data*

IPSL-CM6A-LR (Boucher et al. 2020) is the coupled model developed by the Institut Pierre-Simon Laplace modeling center for phase 6 of the Coupled Model Intercomparison Project

Brought to you by NOAA Central Library | Unauthenticated | Downloaded 01/23/24 09:28 PM UTC

(CMIP6; Eyring et al. 2016). It is composed of the LMDZ6A atmospheric model (Hourdin et al. 2020), the ORCHIDEE land surface model (Krinner et al. 2005) version 2.0 and the NEMO3.6 ocean model (Madec et al. 2017). The atmospheric component has a horizontal resolution of 2.5° × 1.3° on a regular latitude–longitude grid and 79 vertical layers, while the ocean component uses the eORCA1 tripolar grid with a nominal horizontal resolution of 1° refined to 1/3° at the equator, with 75 vertical levels with varying thicknesses. The ocean physics component of NEMO3.6 is coupled to the LIM3 sea ice model (Rousset et al. 2015) and to the PISCES-v2 biogeochemical model (Aumont et al. 2015). The oceanic equation of state is estimated with a polynomial representation of TEOS-10 (Roquet et al. 2015); the model prognostic fields are thus Conservative Temperature and Absolute Salinity. All results are presented for Conservative Temperature, but for simplicity we will simply use the generic term "temperature" in the remainder of the paper.

An ensemble of extended historical simulations was performed with the IPSL-CM6A-LR model [see Bonnet et al. (2021a) for the presentation of the ensemble], following the CMIP6 protocol for the historical period 1850–2014 and extended to 2059 following the ssp245 scenario—apart from the ozone field, which was kept constant to its 2014 values due to missing forcings at the time when the extensions were performed. The ensemble has 32 members, initialized at different branch points of a long preindustrial control experiment (piControl) performed for CMIP6, spaced 20–40 years apart so that the ensemble samples the phases of the low-frequency variability present in the model [see Boucher et al. (2020) or Jiang et al. (2021) for a description of this long-term variability]. In the extended period (2015–59), some files were missing for members r2i1p1f1 and r16i1p1f1, so we only considered the other 30 members for the analysis on the entire period.

The piControl simulation in IPSL-CM6A-LR (run for 2000 years: 1850–3849) has a quasi-linear cooling drift in global mean ocean temperature (corresponding to a heat flux of about -0.13 W m^{-2}), particularly marked below 2000 m, originating from a mean net surface heat loss (Mignot et al. 2021). This drift is propagated in the historical simulations and strongly influences the temperature evolution of the deep ocean, temporarily masking the warming signals, which is thus detrimental to the goals of this study. Removing this drift in ocean temperature outputs is necessary in the post-processing before analyzing any long-term changes. We fitted a second-order polynomial to the 2000-yr piControl annual means at every grid point. Fitting over the longest possible period allows us to isolate the drift without mistakenly picking low modes of internal variability (such as the bicentennial mode in the North Atlantic present in the model; Jiang et al. 2021) (Sen Gupta et al. 2013). We remove the corresponding 210-yr period of this quadratic fit from every member, that is, on each member's respective period of the piControl, and add the same mean state back to each member. This mean state is defined as the mean of the piControl calculated over the period when the historical-extended simulations were performed, 1870–2680. This mean state is added so as to keep full physical values of temperature as opposed to anomalies after removing the quadratic fit. Note that with this procedure all 30 members are ensured to only differ by their phasing of internal variability set by the initial conditions from the piControl. The spread across all 30 members thus better reflects these differences in phasing of internal variability, as opposed to before the de-drifting procedure when the members all had shifted mean states due to their initialization in the drifting piControl (see Silvy 2022, chapter 2).

Large ensembles are useful tools to isolate the forced response from internal variability of the climate system, by averaging across multiple members sampling the uncertainty in internal variability (e.g., Deser et al. 2020). Internal variability can thus be estimated by the intermember spread (usually measured by its standard deviation), a measure that varies over time, as opposed to estimating the internal interannual variability from a piControl that is fixed in time. One advantage of estimating a time-dependent internal variability stems from the fact that it can be impacted in future scenarios compared to the late nineteenth century, which is particularly true in the IPSL-CM6A-LR large ensemble where the spread is reduced (Bonnet et al. 2021a), highlighting an influence of anthropogenic external forcings on internal modes of variability.

b. *Patterns of temperature and heat content changes*

Here, we present the ensemble mean change in vertically integrated ocean heat content (OHC) and zonal mean temperature (Figs. 1a,b), with the corresponding signal-to-noise ratio (SNR; Figs. 1c,d). The "signal" is here defined as the ensemble mean, and the "noise" as the intermember standard deviation. The time of emergence (ToE) is also calculated for each of the 30 members as the time when the SNR last exceeds and remains above a chosen significance threshold (i.e., the time when the forced signal can be unambiguously distinguished from internal variability). Each member's SNR is calculated as the anomaly relative to 1850–99 (the signal) divided by the intermember standard deviation (the noise). The ensemble median ToE is presented (Figs. 1e,f) for a SNR threshold of 3.

Figures 1a and 1b show a broad-scale warming in the ensemble mean by the mid-twenty-first century, particularly pronounced in the subpolar North Atlantic and at the northern bounds of the ACC. The subsurface maximum warming penetrates deepest in the Southern Hemisphere subtropical gyres and in the Arctic (down to about 1000 m). In addition, a weaker but significant warming signal (greater than twice the intermember noise; Fig. 1b) penetrates along the Antarctic Bottom Water (AABW) formation region and ventilation pathway (Fig. 2). On the opposite hemisphere, a subsurface (below 1000 m) cooling is apparent in the deep convection region of the Greenland Sea between 65° and 80°N (Fig. 1b), but it is weaker than internal variability for vertically integrated OHC (Fig. 1a) as the subsurface cooling is mixed with upper-ocean warming. Another cooling region appears around 55°–60°S mainly in the South Pacific sector and also slightly in the Southern Atlantic (Fig. 1a; see also Fig. 1 in the online supplemental material). These cooling regions are associated with deep cooling of very old water masses in the

Brought to you by NOAA Central Library | Unauthenticated | Downloaded 01/23/24 09:28 PM UTC

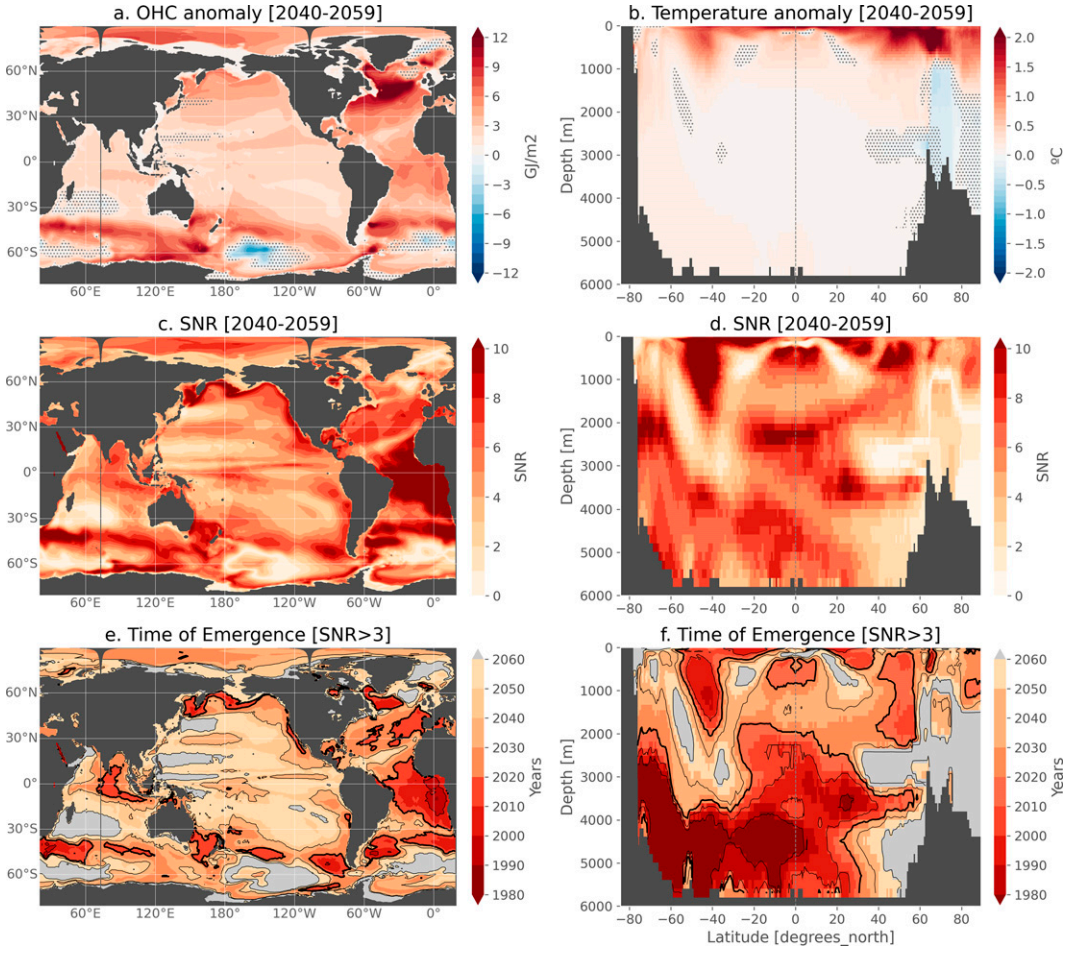

FIG. 1. (a),(b) IPSL-CM6A-LR ensemble mean anomaly relative to 1850–99 and (c),(d) signal-to-noise ratio averaged between 2040 and 2059 (last 20 years of the historical-extended period) for ocean heat content in (a) and (c) and zonal mean temperature anomaly in (b) and (d). (e),(f) Ensemble median time of emergence for a SNR $>$ 3 (gray shading indicates the signal has not emerged in the large ensemble for the chosen threshold; thick black line indicates year 2020). Stippling in (a) and (b) indicates where the anomaly is below twice the intermember standard deviation.

model (water masses that have not been ventilated after 200 years of simulation; Fig. 2). The overall regional patterns of OHC change are consistent with the multimodel mean CMIP5 and CMIP6 projected changes (Fox-Kemper et al. 2021).

Regions with the largest warming signal are not always those with the highest SNR. For instance, the warming in the tropical Atlantic stands out with a very large SNR exceeding 10 for vertically integrated OHC (Fig. 1c), because although the signal of change is not the largest, it is very large relative to the very weak noise of the region, particularly at depth (see Fig. 1d and supplemental Fig. 1 for the basin zonal means). Similarly, the weak warming in the AABW (Fig. 1b) is in fact relatively pronounced in the subsurface when compared to the region's low internal variability (Fig. 1d). The largest pattern of maximum SNR (>10) is located in the subtropical Southern Ocean along the ventilation pathway of SAMW and AAIW, reaching almost 2000-m depth.

For a threshold of 3 for the SNR, a large portion of the Atlantic as well as the Southern Ocean band around 40°–50°S emerges between the late twentieth century and the early twenty-first century. A narrow band along the North Pacific coasts and the Bering Strait also sees an early emergence of its warming pattern, as well as the eastern tropical Indian Ocean due to weak internal variability there (Fig. 1e). The zonal mean view (Fig. 1f) highlights the AABW in the deep and abyssal ocean as the most sensitive water masses, with a warming signal emerging earlier than the 1980s, although it is also where the intermember spread in the ToE is the largest (>100 years for the full ensemble spread; see supplemental Fig. 1). This is a sign that in this region, internal variability acts to modulate the slowly increasing forced signal over the twentieth century and possibly delay or advance its emergence in individual realizations. A larger SNR threshold could be better suited to more coherently detect the forced signal in the full ensemble, with smaller spread. This point will be

Brought to you by NOAA Central Library | Unauthenticated | Downloaded 01/23/24 09:28 PM UTC

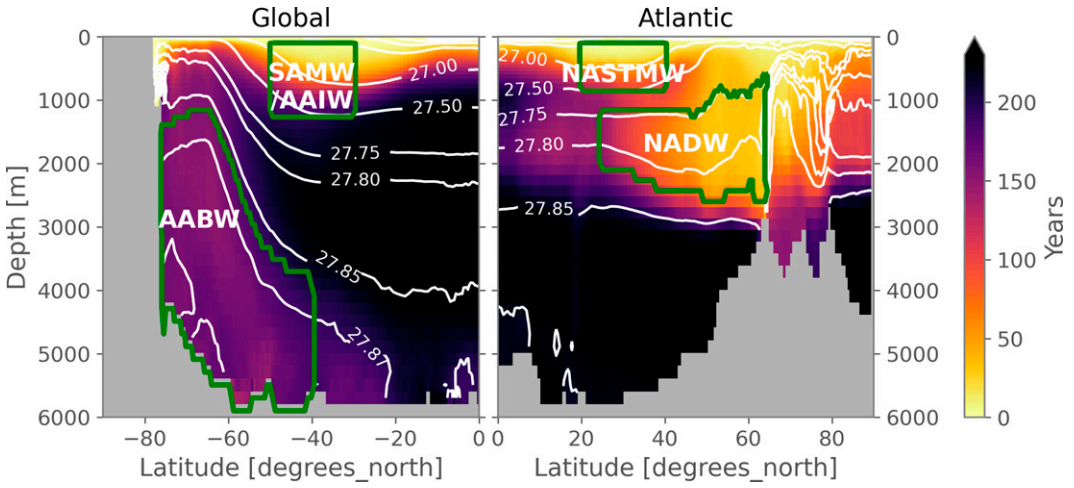

FIG. 2. Zonal mean age tracer in the CTL experiment averaged over the last 20 years (2081–2100) (colors) and potential density (white contours; kg m^{-3}). The age passive tracer is initialized at 0 at the start of the simulation and incremented by one year every simulated year everywhere outside of the mixed layer. The four regions considered for the temporal analysis are drawn in green, corresponding broadly to the range of Antarctic Bottom Waters (AABW), Subantarctic Mode, and Antarctic Intermediate Waters (SAMW/AAIW), North Atlantic Subtropical Mode Waters (NASTMW), and North Atlantic Deep Waters (NADW).

further discussed in section 5. Near the surface, the strong warming in subtropical mode waters emerges before 2020 in both hemispheres, and early emergence before year 2000 is found at around 45°S at 1000-m depth [consistent with Silvy et al. (2020)]. The emerging pattern before 2020 between 45° and 60°N penetrating down to 2000 m (Fig. 1f) is located in the Greenland and Irminger Seas (Fig. 1e), where deep convection occurs in the IPSL-CM6A-LR model (Boucher et al. 2020; Jiang et al. 2021). Regions of no emerging signal (i.e., where the SNR has not exceeded 3 before 2059) include the poorly ventilated lower Circumpolar Deep Water (CDW) where a slight cooling or delayed warming is identified, the surface waters near the Antarctic coast, and the deep ocean north of 40°N.

We are now interested in deciphering which processes cause these different patterns of change and their time scales of emergence from internal variability in the large ensemble, and start with the description of ocean-only simulations, which were specifically designed to address this question.

3. Experimental design

We use the ocean physics component (OPA) of the NEMO3.6 model (Madec et al. 2017), which is the ocean component of the IPSL-CM6A-LR coupled model (thereafter referred to as IPSL-CM6) presented above, under the same eORCA1 configuration, without the sea ice model and the biogeochemical model. The goal of the modeling experiments is to reproduce the ocean response of the historical+ssp245 simulations in the IPSL-CM6 model (over the period 1850–2100) and then decompose that response into separate processes. Namely, we target the contributions from individual surface flux changes on the one hand, and the contributions from the passive transport of added heat and the redistribution of pre-existing heat by the changing ocean transport processes on the other hand. The protocol, configuration, and validation of the simulations are described in detail in a companion paper (Silvy et al. 2022), so here we briefly summarize the experimental design. Since the protocol is closely related to the ocean-only Flux-Anomaly-Forced Model Intercomparison Project (FAFMIP) protocol (Todd et al. 2020), we try to use similar terms, when relevant, to describe our experimental design.

a. Numerical experiments

We first set up a control experiment (CTL; see Fig. 3) with the ocean-only model, forced at the ocean interface with the fluxes from the piControl experiment of the IPSL-CM6 model. The CTL is initialized from the piControl initial state, which itself starts after a multicentury spinup of the coupled model. The surface fluxes from the piControl are outputted on the oceanic grid at 3-hourly frequency (at the ocean–atmosphere and ocean–sea ice interface), twice the coupling frequency. They are prescribed to the ocean-only model with no restoring: the ocean model is therefore forced with fixed fluxes. The high frequency of the forcings enables our CTL experiment to reproduce the internal variability and mean state of the coupled piControl surprisingly well with no deviation during the 251 years of simulations (Silvy et al. 2022).

We then set up the ALL experiment, which is configured exactly like the CTL, except that we now add a perturbation component to each surface flux (heat, freshwater, salt, wind stress) to reproduce the externally forced response in the historical+ssp245 simulations. The perturbations for each flux component are taken as the ensemble mean anomaly relative to 1850–99 from the IPSL-CM6 historical-extended simulations for the period 1850–2059 and ssp245 scenario simulations for the rest of the twenty-first century (2060–2100, 11 members), at monthly frequency. By averaging across members, these perturbations isolate the externally forced historical+ssp245

Brought to you by NOAA Central Library | Unauthenticated | Downloaded 01/23/24 09:28 PM UTC

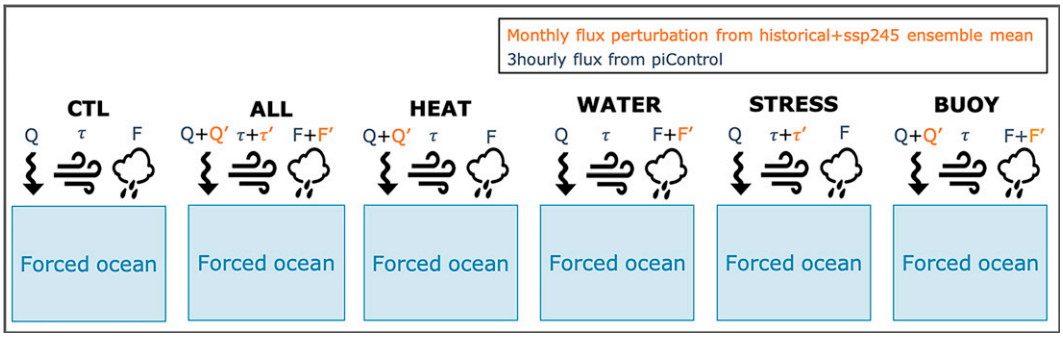

FIG. 3. Schematic of the fixed-flux forced ocean experiments.

response in IPSL-CM6. Maps of the surface flux perturbations are shown in supplemental Fig. 2 averaged over the last 20 years (2081–2100). The ALL experiment thus has the internal variability of the CTL experiment (inherited from the piControl 3-hourly surface fluxes) and the time-evolving externally forced response from the historical+ssp245 simulations (inherited from the monthly perturbations over 1850–2100). ALL thus acts as any historical+ssp245 member, with its own initial conditions from a piControl state, and reproduces the response of the ensemble, which is within the ensemble spread [see Figs. 5, 7, 8, and 9, as well as more diagnostics in Silvy et al. (2022)].

Sensitivity experiments are in turn conducted with the same configuration (Fig. 3), applying the perturbations on the surface heat fluxes only (HEAT), freshwater and associated salt fluxes (WATER), both buoyancy fluxes together (BUOY), and wind stress components (STRESS) respectively. These experiments allow for the total ocean response to be decomposed in separate contributions from individual surface fluxes, within the hypothesis of linear additivity of the components [e.g., the hypothesis that ocean temperature changes in ALL is the sum of temperature changes in HEAT, WATER, and STRESS (or BUOY and STRESS)]. The validity of the linear additivity and its limits are addressed in section 4.

As indicated above, all ocean-only experiments have similar internal variability because of the 3-hourly fixed fluxes from the piControl, so they are directly comparable. All anomalies in the analysis are computed relative to the CTL on the same period of time, filtering out a majority of the internal variability. We note that since this internal variability is inherited from a piControl simulation, it is not affected by the external forcings' eventual impact on modes of variability, unlike what occurs in the scenarios of the twenty-first century, illustrated by a reduced intermember spread in the large ensemble on some variables of the climate system (Bonnet et al. 2021a).

All the experiments also inherit the cooling drift present in the piControl. As for the temperature field in the historical-extended simulations, the drift is removed from the experiments; that is, the corresponding period of the 2000-yr quadratic fit on the 3D temperature field is subtracted and the CTL mean state is added back to all the simulations.

Because there is no sea ice component in the flux-forced experiments, temperature can locally fall below the freezing point in polar regions. We implement a treatment to the equation of state in these regions based on Todd et al. (2020), so that there is no impact of below-freezing temperatures on the dynamics. This point is further discussed in Silvy et al. (2022), with additional sensitivity simulations.

One of the main differences of our protocol with the ocean-only FAFMIP design (Todd et al. 2020) is in the surface perturbations we impose: FAFMIP provides monthly anomalies with no interannual variations, extracted from a multimodel mean in CMIP5 1pctCO2 experiments at a time when CO_2 concentration in the atmosphere has doubled. They impose an idealized step forcing and can thus explore after a relatively short integration time the semi-equilibrium response. Here, we impose on an ocean-only model the perturbations extracted from the historical+ssp245 transient simulations in the IPSL-CM6 ensemble (which has the same ocean configuration as the stand-alone ocean component). This enables us to reproduce the response of these transient coupled simulations, with realistic historical and future external forcings.

b. *Passive tracer and decomposition of temperature changes*

Another goal of this study is to decompose the temperature anomaly T' in the ocean-only perturbed experiments relative to CTL into a contribution T'_a solely due to the addition of surface heat Q', advected and mixed in the ocean without affecting the circulation, and a contribution T'_r created by the redistribution of CTL temperature in response to the perturbed circulation, so that $T' = T'_a + T'_r$. To virtually decompose these two effects, we introduce a passive temperature tracer as in Banks et al. (2002), Banks and Gregory (2006), and other subsequent studies. This passive "added heat" tracer T'_a is initialized at zero, forced at the surface by the same anomalous heat flux Q' as T', and advected by the CTL + perturbed components of the circulation without affecting the circulation itself. Thus, integrated over the global ocean, T'_a amounts to the same storage of heat as T', but their local patterns can differ. The "redistributed heat" is diagnosed in the post-processing by $T'_r = T' - T'_a$ and represents the effect of the perturbed circulation redistributing the background temperature.

Note that T'_a is implemented similarly in each experiment, including CTL. That is, it is forced by Q' (identical to the

Brought to you by NOAA Central Library | Unauthenticated | Downloaded 01/23/24 09:28 PM UTC

surface heat flux perturbation applied in ALL, HEAT, and BUOY) and advected passively by the circulation specific to each experiment), so that T'_a in the perturbed experiments and T'_a in CTL differ only by the effect of the perturbed circulation acting on the added heat. We refer to this component as the nonlinear added heat, diagnosed by $T'_a - T'_a|_{\mathrm{CTL}}$. The definition and implementation of this passive tracer is presented in more detail in Silvy et al. (2022).

To summarize, in the experiments where an anomalous surface heat flux is imposed (ALL, HEAT, BUOY), we can decompose the total temperature change T' (diagnosed from the output prognostic temperature field) into the following:

- an added heat component, diagnosed from T'_a calculated online, further decomposed into a passive heat component, diagnosed from T'_a in CTL: $T'_a|_{\mathrm{CTL}}$,
- the effect of the perturbed circulation on the added heat (what we refer to as the nonlinear added heat component), diagnosed from $T'_a - T'_a|_{\mathrm{CTL}}$, and
- a redistributed heat component, diagnosed from $T' - T'_a$

so that

$$\underbrace{T'}_{\text{total}} = \underbrace{T'_a}_{\text{added}} + \underbrace{T' - T'_a}_{\text{redistributed}}$$
$$= \underbrace{T'_a|_{\mathrm{CTL}}}_{\text{passive}} + \underbrace{T'_a - T'_a|_{\mathrm{CTL}}}_{\text{non-linear added}} + \underbrace{T' - T'_a}_{\text{redistributed}} \quad (1)$$

4. Decomposition of the long-term changes in the ocean-only experiments

Here, we present the decomposition of the long-term ocean warming patterns into contributions from individual surface flux perturbations (Fig. 4; see also supplemental Fig. 3 for the basin zonal means) and into contributions from the added and redistributed components in the ALL experiment, as described above (Fig. 5; see also supplemental Fig. 4 for the decomposition in the HEAT experiment). We show the anomaly averaged in the last 20 years of the simulations compared to CTL in order to maximize the signal magnitude and to compare it with previous studies that used strong idealized forcings. We highlight here the main features that are common to past studies, to set this work in the light of past efforts, before adding new aspects in the next section.

First, we note that the ALL experiment reproduces faithfully the response of the IPSL-CM6 ensemble (Figs. 1a,b and 4a,b), which fulfills its primary purpose. The validation of this ocean-only ALL experiment with respect to the coupled model ensemble is further discussed in Silvy et al. (2022).

The heat flux perturbation explains the overall warming of the ocean as well as its main patterns, as illustrated by the HEAT and ALL experiments (Fig. 4). Yet, some regional differences stand out, particularly in the North Atlantic and in the Southern Ocean, which is evidence for a nonnegligible role played by other flux perturbations in setting the total warming patterns.

In the Southern Ocean, the wind stress perturbation alone (Figs. 4g,h) causes a redistributive warming around 40°–60°S, mostly pronounced in the Atlantic and western Pacific Ocean, penetrating deeply in the ocean and surrounded by cooling patterns at lower and higher latitudes. These results are consistent with previous studies, which explained this warming pattern by the increased northward Ekman transport in response to the poleward and intensifying westerly winds and consistent with an intensification of the wind-driven upper cell (Fig. 6b), acting to transport and subduct more heat north of the ACC (Fyfe et al. 2007; Armour et al. 2016; Gregory et al. 2016; Liu et al. 2018; Garuba and Klinger 2018; Todd et al. 2020; Shi et al. 2020). The northward Ekman pumping and ventilation can also be shifted to slightly higher latitudes in response to the wind stress perturbation (Waugh et al. 2019), creating the dipole pattern in the Indian Ocean (Fig. 4g; cooling at 20°–30°S and warming at 40°–50°S). In southern high latitudes, the freshwater flux perturbation alone causes an intense redistributive cooling in the surface layers and a redistributive warming below from 500 m to the bottom, especially intensified south of 60°S (Figs. 4e,f). This dipole has been explained by increased precipitation at high latitudes in the Southern Ocean, acting to stratify the surface layer, reducing vertical mixing between the upper and deep layers, decreasing the supply of cold newly formed waters into the deep and abyssal layers which causes a redistributive subsurface warming and surface cooling (Gregory et al. 2016; Armour et al. 2016; Todd et al. 2020). This is consistent with the decrease of more than 8 Sv in the Southern Ocean deep overturning cell found at the end of the WATER experiment (Fig. 6c), also found by Todd et al. (2020) with model-dependent rates. The wind stress perturbation has an opposite effect as it acts to strengthen the deep overturning cell (with a peak of 4 Sv in 2060; Fig. 6c), cooling the waters in the subsurface southern high latitudes and along the export pathway of AABW (Fig. 4). We will explore the temporal response of these regional features in more detail in section 5.

More globally, there is a widespread surface cooling in the WATER experiment (Fig. 4f), also found by Gregory et al. (2016), among others, on top of a global subsurface warming. This cooling is consistent with increased stratification caused by the surface freshening in the subpolar Southern Ocean, as mentioned above, since surface waters are colder. Inversely, at midlatitudes where the water column is thermally stable, the surface cooling could be caused by an increase in evaporation over precipitation (supplemental Fig. 2), acting to destratify the water column and enhancing vertical mixing, thus cooling surface waters and warming the subsurface.

In the North Atlantic, the wind stress perturbation is about 4–5 times smaller than in the Southern Ocean (supplemental Fig. 2) and causes only small changes compared to internal variability, such as the warming south of Greenland (Fig. 4g). We note there is no consensus between models in response to the FAFMIP wind stress perturbation in this region in Todd et al. (2020). The freshwater flux perturbation causes a much more significant warming than wind stress perturbation in the North Atlantic basin (greater than internal variability), particularly intensified at 45°–50°N, counteracting the subsurface cooling in HEAT at these latitudes (cf. Figs. 4e and 4c), and a cooling in

Brought to you by NOAA Central Library | Unauthenticated | Downloaded 01/23/24 09:28 PM UTC

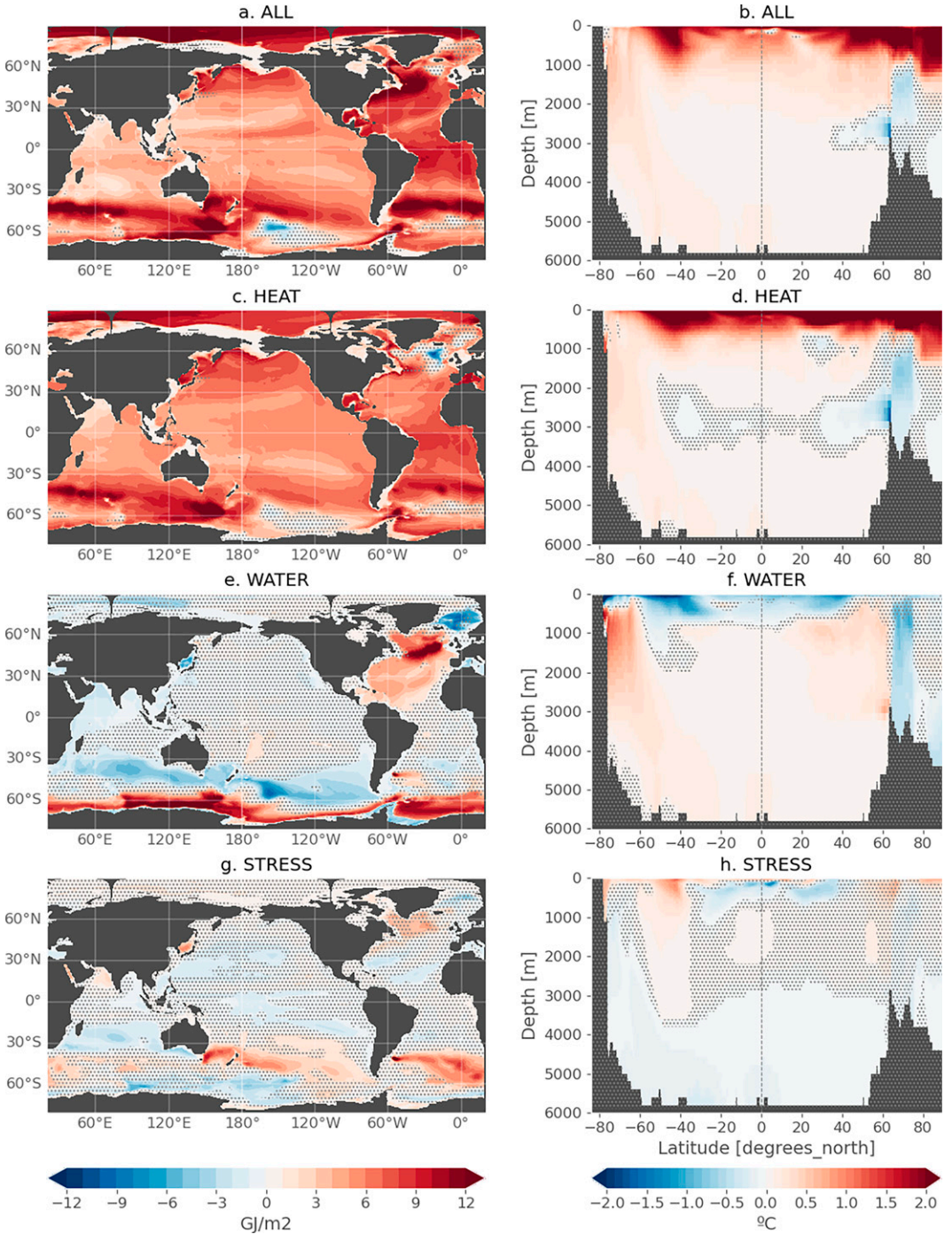

FIG. 4. Ocean heat content and zonal mean temperature anomaly in the ocean-only experiments, for the period 2081–2100 relative to the CTL experiment for the same period. Stippling indicates where the anomaly is below twice the interannual standard deviation of the CTL.

the Nordic seas that propagates on the entire water column (Fig. 4f). This dipole is also present in the multimodel mean of Gregory et al. (2016) in their "faf-water" experiment, although the cooling spreads south of Greenland reaching 45°N. The response to faf-water in Todd et al. (2020, their Fig. 13) reveals that the response patterns in the North Atlantic are very model dependent. The North Atlantic is also found to be the region of largest intermodel spread in total redistributed heat, possibly related to the spread in the magnitude of AMOC weakening (Todd et al. 2020; Couldrey et al. 2021).

Brought to you by NOAA Central Library | Unauthenticated | Downloaded 01/23/24 09:28 PM UTC

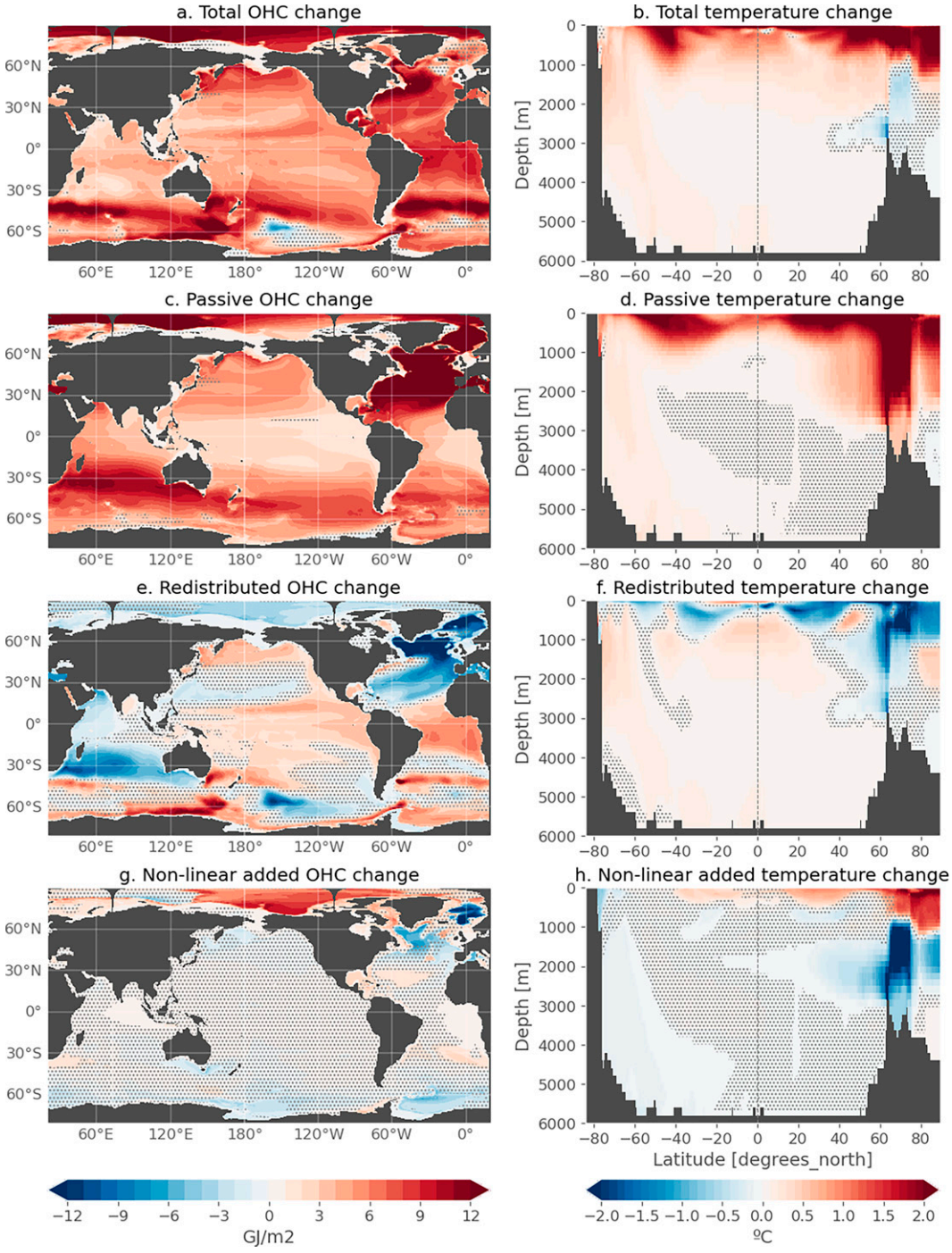

FIG. 5. Ocean heat content and zonal mean temperature anomaly in the ALL experiment for the period (2081–2100) relative to the CTL experiment: (a),(b) total change, (c),(d) passive component, (e),(f) redistributed component, and (g),(h) nonlinear part of the added component (i.e., perturbed transport acting on added heat). Stippling indicates where the plotted field is below twice the interannual standard deviation of the CTL.

As the climate system is inherently nonlinear, some nonlinearities arise from the interactions between the different surface perturbations. These are presented in Fig. A1 and discussed in the appendix. Overall, the largest nonlinearities are found in subpolar areas where there are intense and different ventilation changes between the experiments. Caution should be considered when decomposing the total response in these areas, in that the sum of responses from individual forcings is not exactly equal to

Brought to you by NOAA Central Library | Unauthenticated | Downloaded 01/23/24 09:28 PM UTC

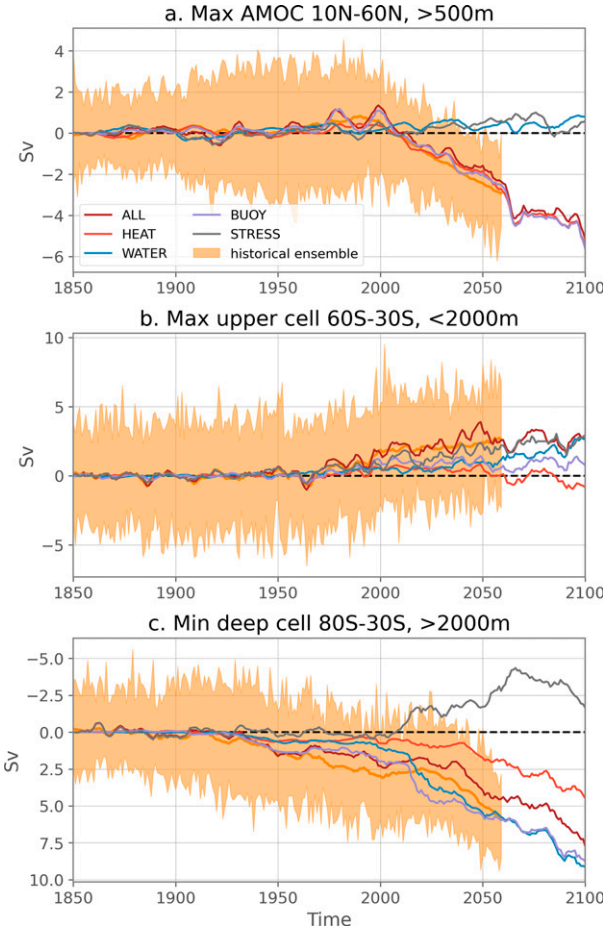

FIG. 6. Time series of circulation anomalies. (a) AMOC (maximum of the Atlantic meridional streamfunction between 10° and 60°N, below 500 m. (b) Southern Ocean upper cell (maximum of the global meridional streamfunction between 30° and 60°S above 2000 m. (c) Southern Ocean deep cell (minimum of the global meridional streamfunction between 30° and 80°S below 2000 m. We take the minimum as the deep cell turns anticlockwise, so has a negative sign. A positive anomaly thus means a decrease in the deep cell, so the *y* axis is reversed.) In the ocean-only simulations (colored lines) the anomalies are relative to the CTL experiment, with a 5-yr running mean applied for visual purposes. The anomalies in the large ensemble (orange shading) are expressed relative to 1850–99.

the all-forcing response, although the decomposition is still relevant to investigate the potential different mechanisms and their respective time scales.

The passive warming component ($T'_a|_{CTL}$; Figs. 5c,d) follows the shape of the main ocean ventilation pathways (see shading of the seawater age tracer in Fig. 2); that is, we see some intense warming (>2°C) along the subtropical gyres and along deep convection regions in the subpolar North Atlantic and Nordic seas. Weaker but significant passive warming (compared to internal variability) is also exported down the AABW pathway. However, circulation changes in the ALL experiment act to decrease the penetration of the added heat in the subsurface (Fig. 5h; nonlinear added heat term, $T'_a|_{ALL} - T'_a|_{CTL}$): because of the upper ocean stratification, the added heat $T'_a|_{ALL}$ is partly trapped at the surface compared to $T'_a|_{CTL}$.

Although the passive component sets the main patterns of total warming, redistributed warming plays a key role in setting some more regional features. First, we note that the main patterns of redistributed change come from the heat flux perturbation (supplemental Fig. 4), meaning that the total HEAT patterns shown in Figs. 4c and 4d arise from a mix of passive and redistributive processes. A notable regional exception is the redistributive cooling pattern in the subtropical gyres (Fig. 5f), particularly intense in the North Atlantic and southern Indian subtropical gyres around 30°S (Fig. 5e; also, see basin zonal means in supplemental Fig. 3). This redistributive cooling is set by all three flux perturbations (WATER, STRESS, and the redistribution in HEAT) and counteracts a strong passive warming in the subtropical gyres. This passive warming is also particularly intensified in the North Atlantic gyre and southern Indian gyre, two important regions for ocean ventilation by subduction of newly formed mode waters (Hanawa and Talley 2001; Morrison et al. 2022).

As in previous work, we find some redistributive warming at low latitudes, in the Atlantic and Pacific basins (Fig. 5e). Some studies have attributed this to an anomalous positive equatorward heat transport, considering both the AMOC weakening and the increased northward Ekman transport in the Southern Ocean (Xie and Vallis 2012; Winton et al. 2013; Gregory et al. 2016; Garuba and Klinger 2018; Hu et al. 2020; Bronselaer and Zanna 2020; Todd et al. 2020; Dias et al. 2020; Couldrey et al. 2021). However, it seems that this vertically integrated redistributive warming around the equator arises not only from the upper ocean but also from significant warming in the entire water column below 500 m (Fig. 5f). This subsurface redistributive warming can be attributed both to the redistributive component of the heat flux perturbation (supplemental Fig. 6f) and to the freshwater flux perturbation (Fig. 4f).

In the North Atlantic, there is a strong passive warming component extending from the subtropical gyre to the Nordic seas (Fig. 5c), due to the positive surface heat flux perturbation (supplemental Fig. 2), partly compensated by a redistributive cooling in line with the AMOC weakening (Fig. 6a) and particularly intense in the subsurface (Fig. 5f), consistent with previous studies (Banks and Gregory 2006; Xie and Vallis 2012;Winton et al. 2013; Marshall et al. 2015; Gregory et al. 2016; Garuba and Klinger 2016, 2018; Todd et al. 2020; Bronselaer and Zanna 2020; Williams et al. 2021; Couldrey et al. 2021).

The overall agreement in the decomposition of the total temperature response to increasing anthropogenic forcings with previous findings under different or more idealized setups validates the coherence of our ocean-only experiments.

5. Temporal response in the main ocean ventilation pathways

We now aim to explore the processes and the time scales that drive anthropogenic heat storage in the ocean interior. We thus proceed to investigate the temporal response of the contributions discussed above, in four significant regions for

Brought to you by NOAA Central Library | Unauthenticated | Downloaded 01/23/24 09:28 PM UTC

ocean ventilation. We have seen the important role played by the North Atlantic and Southern Ocean in setting ocean heat uptake patterns, not surprising considering their prominence for the global ocean overturning circulation.

First, we will focus below on upper ocean ventilation (upper two green boxes in Fig. 2), associated with the subduction of mode and intermediate waters feeding the subtropical gyres. We look at the region entitled "SAMW/AAIW" in the Southern Ocean (indicating Subantarctic Mode Waters and Antarctic Intermediate Waters), in a zonal average framework. These water masses feed the upper limb of the Southern Ocean upper cell, subducting surface properties and changing along their way (Morrison et al. 2022). In the North Atlantic, we look at the North Atlantic Subtropical Mode Waters (NASTMW), also known as Eighteen Degree Waters (Talley and Raymer 1982). These two regions are very well ventilated in the model, as seen by the seawater age tracer (Fig. 2).

Next, we will focus on the export pathways associated with the formation of Antarctic Bottom Waters (AABW) and North Atlantic Deep Waters (NADW) (see the lower two green boxes in Fig. 2). AABW and NADW are the two most prominent water masses found in the ocean (Johnson 2008), feeding the lower limbs of the MOC. They flow equatorward from their formation region, occupying the abyssal and deep layers respectively, before being mixed with surrounding overlying water masses or transported upward by wind-induced upwelling (Marshall and Speer 2012). Note that we adopt an Eulerian view, with fixed geographical regions, to investigate how these climatologically well-ventilated areas of the ocean are affected in their heat storage response by different types of change, along with the time scales of emergence of these forced signals from internal variability. We leave a more specific water mass tracking framework (e.g., Sallée et al. 2013) for potential future work.

a. *Upper-ocean ventilation*

We present the evolution of temperature anomaly averaged in the SAMW/AAIW and NASTMW regions in Fig. 7. The total warming is shown by the dark red curve representing the ALL experiment and by the orange spread representing the large ensemble. The ALL response in the SAMW/AAIW region is well within the spread of the large ensemble and has a similar evolution as the ensemble mean. This warming signal in SAMW/AAIW, starting early in the twentieth century, is dominated by added heat ($T'_a|_{\mathrm{ALL}}$, dark red dotted line). It is slightly damped by a small redistributive cooling (difference between the dotted and solid dark red lines). This redistributive cooling stems in the most part from the redistribution caused by the heat flux perturbation (difference between the dotted and solid light red lines), consistent with increased surface stratification preventing the downward spread of heat. Wind stress and freshwater perturbations redistribute heat in such a way that wind stress tends to warm SAMW/AAIW, while freshwater tends to cool them (consistent with Fig. 4), almost compensating each other. But we see here that although their impact on temperature is nonnegligible at the end of the twenty-first century, they start showing an influence on temperature decades after the heat flux perturbation (Fig. 7a).

The total warming significantly emerges at the turn of the century (Fig. 7c). As displayed by the spread in the large ensemble in Fig. 7c, the higher the SNR threshold, the more coherent the ToE in the large ensemble is (i.e., the intermember spread is smaller). This occurs because the warming in the twentieth century is slow and subject to modulations by internal variability, which can delay the emergence by several decades between members. When the warming signal picks up the pace at the turn of the century, the modulations by internal variability are too weak to slow down the forced signal as it did in the twentieth century, and the emergence depends much less on the SNR threshold. All members emerge within a maximum of 35 years of each other for SNR $>$ 5 (1980–2015) and within two decades for SNR $>$ 7 (by 2020). Passive warming emerges earlier than the total response (black triangle in Fig. 7c; identical for the added component in the other simulations; not shown to lighten the figure) by about 15 years for SNR $>$ 5 and SNR $>$ 7, illustrating the effect of the redistribution component in slightly delaying the emergence of the total signal. The passive warming, as well as the response in HEAT and BUOY, still emerges within the large ensemble ToE distribution, which indicates that the effects of the redistributive processes on signal emergence are of the same order of magnitude as the uncertainty of internal variability on the emergence of the forced signal. The cooling in the WATER experiment and warming in STRESS both emerge in the twenty-first century but outside of the large ensemble distribution and with larger gaps between SNR thresholds because of the slower timing of the response.

On the North Atlantic side, the NASTMW region is also dominated by passive warming until the early twenty-first century ($T'_a|_{\mathrm{CTL}}$). Redistributive cooling in the ALL experiment (the difference between the dotted and solid dark red lines) starts to counteract the passive signal in the 2010s and increases in the twenty-first century. This redistributive cooling is largely driven by the heat flux perturbation itself, as illustrated by the redistributed component in the HEAT experiment (the difference between the dotted and solid light red lines, as shown on the right side of Fig. 7b). This is consistent with a heat flux driven stratification tending to decrease ventilation in this region in the early twenty-first century (not shown) and might be related to the concurrent AMOC weakening (Fig. 6a) reducing northward heat transport. In contrast to SAMW/AAIW, the temperature change implied by freshwater and wind stress perturbations is much smaller than the change due to the heat flux perturbation. There is nevertheless a weak cooling due to both these perturbations at the end of the twenty-first century. When combined with heat flux changes, the freshwater flux contribution however appears negligible since in the BUOY experiment (buoyancy flux perturbations combined) the warming is superimposed on the response in HEAT (note that ToEs are also equal in HEAT and BUOY so that the red dots in Fig. 7d are overlaid by the purple ones). This reveals a nonlinearity in the response to buoyancy fluxes toward the end of the twenty-first century (BUOY $\neq$ HEAT + WATER).

Brought to you by NOAA Central Library | Unauthenticated | Downloaded 01/23/24 09:28 PM UTC

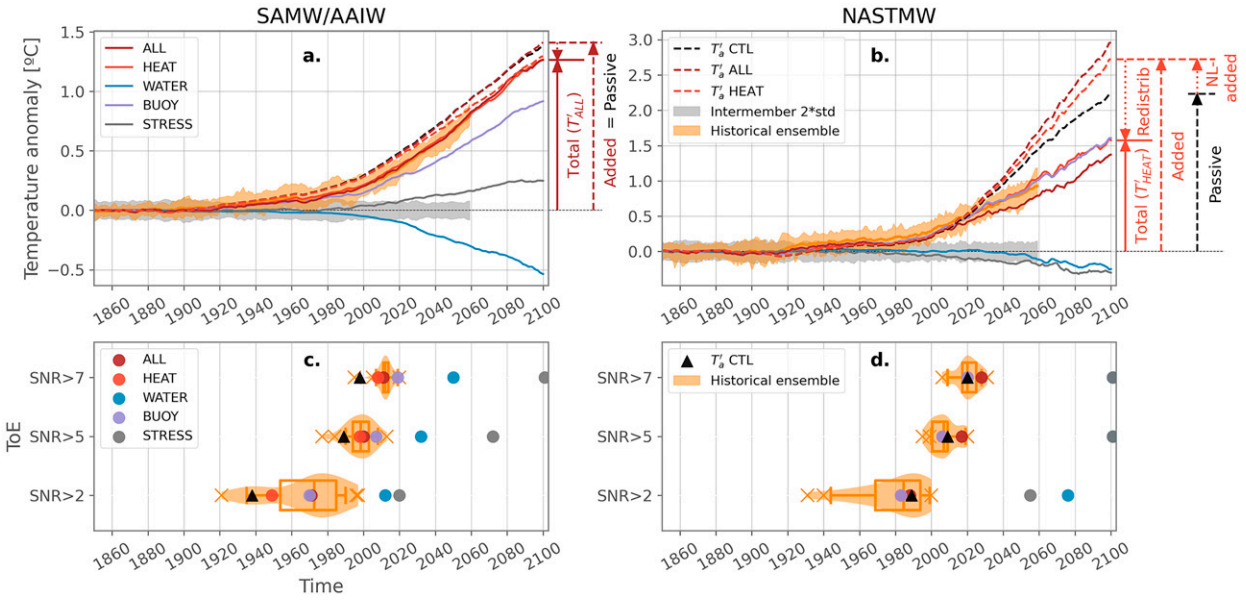

FIG. 7. (a),(b) Temperature anomalies and (c),(d) corresponding ToE at different thresholds in the (left) SAMW/AAIW and (right) NASTMW regions. The orange shading corresponds to the envelope of the large ensemble (LE). Each colored line/circle represents an ocean-only experiment (see legend). Anomalies in the experiments are expressed relative to the CTL at each time step to remove the maximum effects of internal variability, and expressed relative to 1850–99 in the LE [orange shading in (a) and (b)]. The dotted lines in (a) and (b) are T'_a , representing the added heat in CTL (or passive heat; black), ALL (dark red), and HEAT (light red). The difference between T'_a in the perturbed experiments and CTL corresponds to the nonlinear added heat (the effect of the perturbed transport acting on the added heat). The decomposition of temperature changes at the end of the century is shown by the arrows on the right side of the axis for ALL in (a) and HEAT in (b). The ToE is shown only for $T'_a|_{\mathrm{CTL}}$ for visual purposes (black triangle). The gray shading in (a) and (b) is $\pm 2\sigma_{\mathrm{intermember}}$ in the LE temperature (before anomalies are computed), meaning that when a temperature anomaly line crosses that threshold for the last time this corresponds to the ToE for SNR > 2 (we propagate the $\sigma_{\mathrm{intermember}}$ value in 2059 in the last 41 years for signal detection in the ocean-only experiments). The distribution of ToE in the LE is shown both by the orange box plots (whiskers represent the 5th and 95th percentiles of the distribution; outliers are represented by orange crosses) and by the orange shaded violin plots.

The response of the nonlinear added heat component in the ALL experiment ($T'_a|_{\mathrm{ALL}} - T'_a|_{\mathrm{CTL}}$) and its timing are coherent with the decreased ventilation in the region (increased age tracer; not shown), consistent with the increased surface heat flux stratifying the upper ocean, trapping the excess heat near the surface instead of the deeper heat transport in CTL (see also Fig. 5h and supplemental Fig. 7).

Similarly to the SAMW/AAIW region, the large ensemble spread in ToE of the NASTMW warming reduces considerably between SNR thresholds of 2 and 5 (Fig. 7d). The forced signal in the large ensemble has unambiguously emerged for the full distribution by 2020–30 for a SNR > 7. The emergence of the temperature signal is dictated by the heat flux perturbation, which is slightly delayed by redistribution, as indicated by the 10-yr difference in ToE between the passive warming and the total warming (black triangle vs dark red dot for SNR > 5 and SNR > 7). In contrast, the cooling caused by the wind stress or freshwater perturbations alone is barely significant compared to internal variability during the entire simulation (no emergence for SNR > 5), but wind stress perturbations cause the ALL simulation to diverge from the BUOY simulation in the early twenty-first century, postponing the emergence of the warming by about 10 years.

Overall, both regions present a similar temporal response in total warming, with an early signal starting around 1920, a slow increase until the late twentieth century, and a stronger warming trend during the twenty-first century, coherent with the temporal evolution of global mean near-surface air temperature in the model and in observations (Bonnet et al. 2021b), and with global mean SST in the model (Silvy et al. 2022). By the early twenty-first century, the warming of these mode waters is already outside the range of internal variability, with an emergence about 10 years earlier for the Southern Hemisphere compared to the North Atlantic. Redistribution plays a larger role in damping the magnitude of the warming brought by the transport of added heat in the North Atlantic (54% of the added heat in 2100) compared to the Southern Ocean (10%). However, the impact of redistribution occurs earlier in the Southern Ocean, because of the heat flux perturbation acting to weaken the ventilation of the region earlier (as diagnosed by the evolution of the age tracer; not shown). The exact reason for this difference of timing remains to be investigated in detail. Furthermore, while the redistribution is significant in the North Atlantic, its impact in delaying the emergence of the warming is small (about 10 years, even smaller than in the SAMW/AAIW region). There are opposite

Brought to you by NOAA Central Library | Unauthenticated | Downloaded 01/23/24 09:28 PM UTC

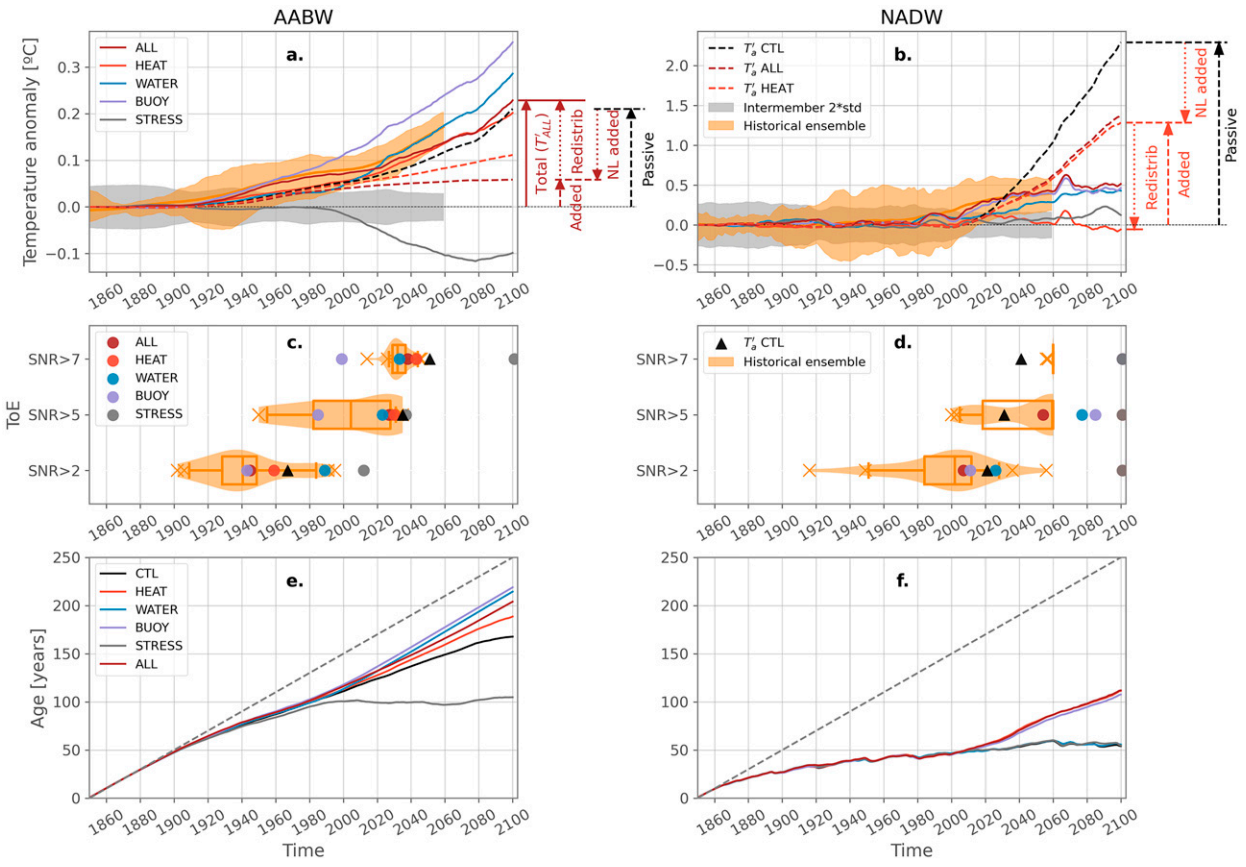

FIG. 8. (a)–(d) As in Fig. 7, but for AABW and NADW. (e),(f) Age tracer in the ocean-only experiments. The gray dotted line represents the values of no ventilation.

effects of the wind stress changes in these two regions, which act to bring more warming in the Southern Ocean versus cooling in the North Atlantic, with an accelerating/slowing effect of about 10 years of the warming and its emergence from internal variability when comparing the all-forcing simulation (ALL) to the simulation without wind stress perturbations (BUOY). In both regions, an SNR of 2 still causes a large spread in the emergence of the large ensemble warming, which is much reduced for a larger threshold. The ~10-yr differences in emergence mentioned above between the different components (e.g., ALL vs BUOY, ALL vs passive warming) correspond to an externally forced difference. Indeed, it is the externally forced signal that is compared both for the temperature changes, since they are expressed relative to CTL, and for the passive tracers since they are forced by the ensemble mean perturbation alone. These ~10-yr differences are comparable to the differences between historical members induced by internal variations, since the spread of ToE in the large ensemble is larger than 20 years (Figs. 7c,d).

b. *Deep water formation and their export pathways*

We now move to the regions associated with the export of AABW and NADW, presented in Fig. 8.

Unlike what occurs in the previous two regions, the AABW warming is due to contributions both from excess heat entering the ocean ($T'_a|_{ALL}$, dark red dotted line), passively transported, and to redistributive processes (difference between dark red solid and dotted lines). The redistributive warming is coherent with a weakening of the deep cell (Fig. 6c) in response to an increase in both the surface freshwater and heat fluxes at southern high latitudes (supplemental Fig. 6). The deep cell weakening is indeed associated with a decrease in the ventilation of the region (Fig. 8e), which prevents newly formed cold waters at the surface from being mixed with the underlying layers, leading to subsurface warming and surface cooling (see Fig. 4f). In the twenty-first century, the redistributive warming is primarily driven by the increased surface freshwater flux into the ocean (which contributes more to the buoyancy flux anomaly than the heat flux perturbation in this region; see supplemental Fig. 8), competing with a redistributive cooling caused by wind stress changes. In contrast to heat and freshwater perturbations, wind stress perturbations result in an increase of the deep cell strength (Figs. 6c and 8a,e). These circulation changes in the twenty-first century are coherent with the evolution of the mixed layer depth (MLD) south of 60°S (Fig. 9a). Indeed, they feature an abrupt shutdown of deep convection in the WATER and BUOY experiments at

Brought to you by NOAA Central Library | Unauthenticated | Downloaded 01/23/24 09:28 PM UTC

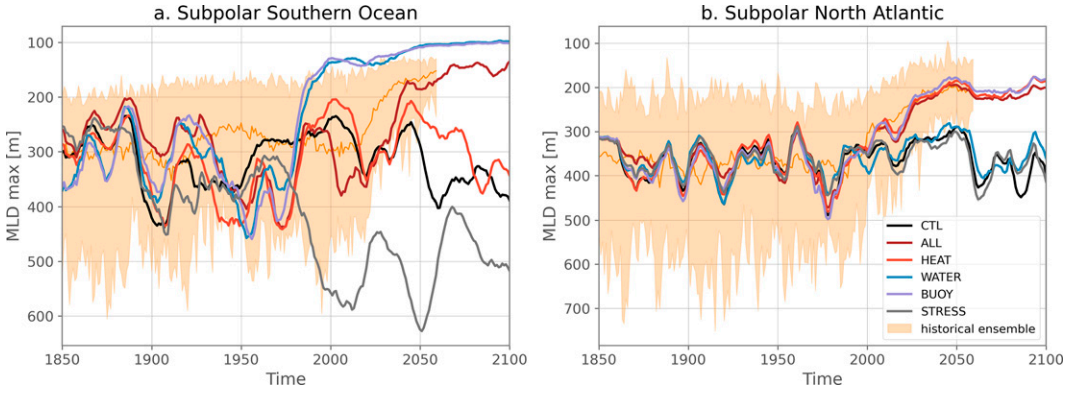

FIG. 9. Mixed layer depth (annual maximum) in (a) the Southern Ocean south of 60°S and (b) the subpolar North Atlantic, in the large ensemble (orange shading) and in the ocean-only experiments (colored lines; with a 10-yr running mean applied for visual purposes). The MLD is defined as the depth at which there is a 0.03 kg m^{-3} difference in potential density relative to 10 m. See supplemental Fig. 8 for the geographical delimitation of the subpolar North Atlantic, and for the time series in more specific deep convection regions.

the end of the twentieth century that is sustained in the rest of the simulations in response to the increased surface freshwater flux. This shutdown is compensated by a MLD deepening in response to the surface wind stress increase (Fig. 9a). As a result of the competing effects between buoyancy fluxes and wind stress, the shoaling of the MLD in the ALL experiment does not show abrupt change but is more gradual throughout the twenty-first century (consistent with the response of the large ensemble; Fig. 9a). In summary, AABW warming results from a combination of added heat at the surface that is transported as part of the deep cell circulation, and reduction of strength of the deep cell. The deep cell slowing itself is caused by a balance of buoyancy fluxes that tend to push toward a rapid shutdown of the circulation, and wind stress change that counterbalances this effect by reinforcing the circulation thereby avoiding a rapid shutdown.

Changes in the AABW actually start early in the twentieth century (Fig. 8a), as indicated by very early ToE (around 1940) when using a SNR threshold of 2 (Fig. 8c). This early emergence can actually be explained by the low noise level in temperature variations characterizing this region. Indeed, a minor change in the circulation—on top of the passive warming slowly entering the ocean—leads to a temperature change that exceeds this noise. This occurs even though the circulation change might be small or temporary (Fig. 6c) and before there is a clear shutdown in deep convection (Fig. 9a). The very large spread in the intermember ToE (almost one century wide for SNR > 2) is a clear indication that the threshold of 2, combined with the slow warming of the twentieth century, is too small to detect emergence of this early signal in all members of the ensemble in this water mass. Even for SNR > 5, the spread of the intermember ToE is large, and it is really only with a threshold of 7 combined with the more rapid forced warming that emergence is unambiguously detected in all members (i.e., small spread in the intermember ToE). This highlights the difficulty of isolating the forced signal in this region before the early decades of the twenty-first century, because of potentially sensitive mechanisms to the different phases of internal variability expressed in the individual members of the large ensemble that modulate the water mass change signal (e.g., Abrahamsen et al. 2019; Silvano et al. 2020). With SNR > 7, the forced signal robustly emerges in the full ensemble by 2040, a timing consistent with the large changes in the circulation associated with the reduction in deep convection and decrease of the deep cell. In this case, the warming in the BUOY experiment emerges outside of the large ensemble distribution, about 40 years before the warming in ALL because in ALL the effects of buoyancy forcing are counterbalanced by the redistributive cooling associated with wind stress perturbations.

We here only discussed AABW changes very close to their sources around the Antarctic continent. But the model shows that AABW warming is transmitted along the export pathway of AABW farther northward in the abyssal ocean, and even spread over the entire deep 2000–4000 m ocean at global scale (supplemental Fig. 7). The timing of circulation from the AABW formation regions to its upward mixing in the 2000–4000-m layer is arguably longer than our simulation (e.g., DeVries and Primeau 2011; Fig. 2). It is therefore surprising to see abyssal warming spreading in the wider ocean at time scales from a few decades to a century. Our analysis presented in supplemental Fig. 9 shows that it is changes in circulation and deep ocean stratification that actually allow for a rapid spread of the climate signal in the deep ocean, with almost no contribution from the added heat passively transported at the century time scale.

The NADW region is much more ventilated than its Southern Hemisphere counterpart (AABW), as illustrated by the age tracer (Figs. 2 and 8e,f). Yet, the warming signal emerges much later—or not at all depending on the SNR threshold. This delay in the warming signal can be attributed to much larger internal variability, as expressed by the large ensemble spread, in addition to the timing and effects of the forced signals themselves. The rise of the passive warming occurs much later, and it is simultaneously counteracted by a redistributed cooling (Fig. 8b) that further delays the warming. Indeed,

Brought to you by NOAA Central Library | Unauthenticated | Downloaded 01/23/24 09:28 PM UTC

strong and rapid passive heat ($T'_a|_{CTL}$) arises starting in the 2000s and emerges after a few decades. The excess heat in the ALL simulation ($T'_a|_{ALL}$) is damped by almost half by 2100 compared to $T'_a|_{CTL}$ because of circulation changes in response to the heat flux perturbation ($T'_a|_{ALL} \approx T'_a|_{HEAT}$). This negative nonlinear added heat component is consistent with AMOC weakening and with the large reduction of deep convection in the subpolar North Atlantic, both driven by the heat flux perturbation (Figs. 6c and 9a; see also supplemental Fig. 8 for more specific time series showing a shutdown of deep convection in the Labrador Sea and decrease in the Greenland Sea). Indeed, these circulation changes lead to a decrease in the overall ventilation of the region (Fig. 8f), preventing added heat in ALL from penetrating as deeply as in the CTL. All of these processes are consistent in terms of timing, starting in the early twenty-first century. Furthermore, the AMOC weakening also explains the large redistributive cooling in HEAT (difference between $T'_a|_{HEAT}$ and HEAT in Fig. 8b), entirely balancing the added heat component ($T'_a|_{HEAT}$), so that the temperature anomaly in HEAT stays around zero for the entire period (Fig. 8b). It is worth noting that once the heat flux perturbation starts to substantially rise in the 2000s (much later than in the AABW; see supplemental Fig. 8), it causes both the added warming and a redistributive cooling through AMOC weakening. Both the delay in the rise of the heat flux perturbation and its effect on the redistribution are implicated in postponing the warming signal in the NADW compared to the AABW.

The wind stress perturbation has almost no effect in this region; however, as for the AABW, the freshwater flux perturbation causes a redistributive warming of almost the same intensity as the ALL warming at the end of the twenty-first century. Nevertheless, the warming in response to the freshwater flux experiment cannot be clearly explained by AMOC, MLD, or ventilation changes as these remain very close to the CTL. This warming is supposedly externally forced since the anomaly is presented relative to CTL, and corresponds in timing to a small rise in the surface freshwater flux anomaly in this region (supplemental Fig. 6). Exact mechanisms still remain to be clarified.

In the large ensemble, the spread in the temperature anomaly is very large throughout the simulation. It only starts to narrow toward the end of the historical-extended period, with no emergence of the ensemble for SNR > 7, the signal being still too weak compared to internal variations.

6. Summary and discussion

In this study, we introduced a new numerical framework [presented in detail in Silvy et al. (2022)] to investigate the time scales of passive and redistributive processes and the role of individual surface flux perturbations on ocean temperature changes in response to climate change. With an ocean-only model forced with fixed (i.e., prescribed), time-evolving fluxes, we proposed a set of experiments to examine the response of the ocean to the externally forced signal of the IPSL-CM6A-LR large ensemble of historical+ssp245 simulations. We force the model with climate change–induced variations in all the buoyancy and wind stress fluxes together, as well as by isolating changes of individual fluxes, in an endeavor to disentangle and understand their respective role. A passive temperature tracer, forced with the heat flux perturbation, was implemented to isolate the signal and time scales of anthropogenically added heat spreading passively in the ocean interior. This numerical framework is particularly adapted to isolate the emergence of externally forced signals relative to internal variability, as all the ocean-only experiments are forced with the same background variability at 3-hourly frequency from a coupled unforced piControl.

Compared to previous studies that investigated these mechanisms under long-term radiative forcing, we focus on the transient response to climate change and on the time scales necessary for the forced signals to emerge from background internal variability. We highlight that the redistributive component becomes increasingly important in shaping the anthropogenic ocean warming signal in some water masses through the course of the twenty-first century. Its influence on the emergence of the warming signal from internal variability thus depends on whether the added component alone emerges before the redistribution can enhance or delay the total signal.

In the mode waters of the midlatitude Southern Ocean and North Atlantic (SAMW/AAIW and NASTMW), circulation changes produce a redistributive cooling that is small in the Southern Hemisphere but significant in the North Atlantic by the end of the century. This redistributive cooling delays the emergence of the total warming signal by about 10 years, which is already distinguishable from internal variability by the early twenty-first century. While the redistributive cooling in the mode waters of the North Atlantic has a significant impact on the intensity of their total warming, it is relatively slow to establish so that circulation changes only have a very minor role on the emergence of the warming.

In contrast to the upper ocean, circulation changes play a key role in warming the deep and abyssal waters of the subpolar Southern Ocean. Indeed, warming in this region results from a combination of added heat that is exported by the deep cell, and deep cell weakening warming the ocean by reducing cold water influx. The two are important and have similar time scales over the twentieth century, but redistribution takes the upper hand over the twenty-first century, as it gets increasingly difficult to passively export the excess heat with the deep cell weakening. The warming induced by circulation changes is driven by a combination of buoyancy flux changes that increase the stratification, therefore shoaling the MLD and reducing ventilation of the deep ocean by cold water, which is counterbalanced by wind stress changes that tend to increase deep convection and ventilation. Overall, all fluxes are important in setting AABW warming: buoyancy fluxes impact both added heat (mostly heat flux) and redistributed heat (mostly freshwater flux), and the wind stress impacts redistribution. The emergence is significantly delayed by the wind stress perturbation starting in the late twentieth century.

While the redistribution component is important for the deep Southern Ocean warming signal to emerge before the added heat alone, the deep North Atlantic waters are cooled by the redistribution component in response to AMOC weakening, significantly counteracting the increasing passive warming in

Brought to you by NOAA Central Library | Unauthenticated | Downloaded 01/23/24 09:28 PM UTC

the twenty-first century. This is explained by an AMOC weakening driven by the heat flux perturbation in the twenty-first century, consistent with a decrease in deep convection found in all convective areas of the subpolar North Atlantic. As a result of these counteracting processes, the residual warming emerges decades later than in the Southern Ocean, or does not emerge with high significance thresholds, unlike its Southern Hemisphere counterpart. The fact that the forced signals (passive warming and AMOC weakening) do not significantly increase before the twenty-first century in the North Atlantic is consistent with a) large internal variability of the region and b) large aerosol radiative cooling in the Northern Hemisphere in the twentieth century, temporarily offsetting the greenhouse gas (GHG) radiative warming (Szopa et al. 2021). Scenario ssp245 is associated with reduced aerosol forcing into the twenty-first century, while GHGs continue to increase (Gidden et al. 2019), so that GHG forcing is not counterbalanced anymore by the aerosol cooling effect. This is consistent with the AMOC temporal evolution, showing only small changes over the twentieth century and decreasing rapidly in the twenty-first century in this model (Fig. 6a) once the heat flux over the North Atlantic starts to increase (supplemental Fig. 6). Such AMOC response is similar to the CMIP5 and CMIP6 multimodel mean (Shi et al. 2018; Menary et al. 2020; Hassan et al. 2021). The impact of aerosols on heat fluxes in the North Atlantic has potential implications for detection and attribution studies of ocean interior changes, delaying the detectability of the observed changes in the North Atlantic, while the Southern Ocean observed warming has already been attributed to anthropogenic forcings, in the SAMW/AAIW but also at greater depths (Swart et al. 2018; Hobbs et al. 2021).

While the decrease in subpolar Southern Ocean deep convection in climate models in response to increasing CO_2 forcing is now well established (Gregory 2000; de Lavergne et al. 2014; Heuzé et al. 2020), how can we trust the time scales of the processes responsible for this deep convection shutdown uncovered here when such climate models do not accurately reproduce the observed processes of AABW formation (Heuzé et al. 2013; Heuzé 2021) or include the amplified Antarctic ice shelf glacial melt contribution, which can significantly impact the ventilation (Lago and England 2019)? Indeed, an accurate representation of shelf processes is missing from global climate models, and although in the case of IPSL-CM6A-LR there might be some dense water formed on the shelf, its export to the deep ocean is uncertain, and most of the bottom waters are formed by deep convection in the Weddell Sea, under sea ice (Heuzé 2021; Mohrmann et al. 2021). As open-ocean deep convection controls the renewal of AABW and overturning circulation in the model world, decreases in this deep convection in response to increased freshwater and heat fluxes might thus lead to too rapid subsurface changes. The influence of the buoyancy fluxes here may be overestimated compared to the perturbation from the winds, which might act to delay the emergence. However, the ice shelf melt, which is not an interactive feature in this and other CMIP models, is expected to amplify the surface freshening and stratification, decrease AABW formation, and progressively warm the subsurface and abyssal ocean waters, which can in turn create a positive feedback on the basal melt (Fogwill et al. 2015; Silvano et al. 2018; Bronselaer et al. 2018; Lago and England 2019). This might tend to move the emergence forward.

In turn, the North Atlantic has been shown to be the most model-dependent region in the response to increased CO_2 forcing and its decomposition into different flux perturbations (Todd et al. 2020; Couldrey et al. 2021). Large sources of heat uptake uncertainties across models have been identified in the spread of surface fluxes and ocean model formulations (Huber and Zanna 2017; Couldrey et al. 2021), leading to large uncertainties in projections of ocean circulation changes (Huber and Zanna 2017; Zanna et al. 2019a; Bronselaer and Zanna 2020).

The different processes discussed in the paper thus make sense for our understanding of future changes; however, the time scales and amplitude on which they occur in the real world, especially in the deeper areas of the ocean, are largely unknown, and remain a large object of uncertainty.

Here, we decompose the response to different drivers of change without allowing any feedbacks between the ocean and other components, as we use an ocean-only model with no sea ice and fixed fluxes. We do this in an endeavor to decouple the components as much as possible and concentrate on the response of the individual flux perturbations actually received by the ocean during the historical+ssp245 period in the coupled model. The balance of processes highlighted here may be different when perturbing an ocean coupled to a sea ice model, which allows feedbacks on the air–sea fluxes (Dias et al. 2021). Subpolar areas are also where the strongest nonlinearities between perturbation fluxes occur, and where, in the absence of a sea ice model, the temperature can fall below freezing point, even though we changed the equation of state so that it does not affect the circulation. These points show the limitation of these experiments in rigorously decomposing physical drivers of change in ice-covered and convective regions, although they bring an understanding of the response to separate processes.

Finally, the sensitivity of ocean warming time scales to initial conditions (large spread in ToE for SNR > 2) uncovered here in the large ensemble suggests that a multiple large ensemble analysis would be a promising approach to identify whether these features are robust across models that have different representations of internal variability, and whether the sensitivity to initial conditions holds in the same regions. Furthermore, conducting similar work with a model ensemble at different spatial resolutions would present an opportunity to explore resolution uncertainty. Both these avenues could help better quantify the uncertainties in time scales of climate signal emergence in the ocean interior.

Acknowledgments. We thank Christian Ethé and Gurvan Madec for all their help in the development of the modeling framework. This work was granted access to the HPC resources of IDRIS under the allocations 2020-A009017403 and 2020-A0080107451 made by GENCI. This work also benefited from the ESPRI computing and data centre

Brought to you by NOAA Central Library | Unauthenticated | Downloaded 01/23/24 09:28 PM UTC

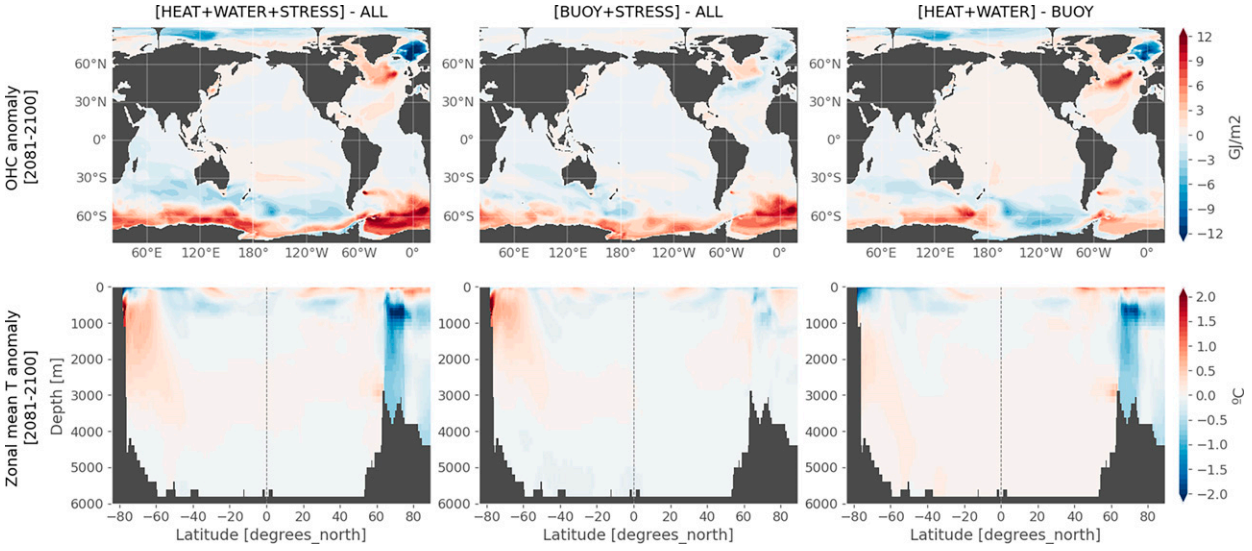

FIG. A1. Differences (left) between the ALL experiment and the sum of HEAT, WATER, and STRESS experiments, (center) between ALL and the sum of BUOY and STRESS, and (right) between BUOY and the sum of HEAT and WATER for ocean heat content and zonal mean temperature anomaly in (2081–2100) relative to the CTL.

(https://mesocentre.ipsl.fr), which is supported by CNRS, Sorbonne University, Ecole Polytechnique, and CNES and through national and international grants. E.G. acknowledges funding from the ARCHANGE project of the "Make our planet great again" program (ANR-18-MPGA-0001, France). J-B.S. acknowledges funding from the European Union's Horizon 2020 research and innovation program under grant agreement 821001.

Data availability statement. The code modified for the development of the numerical experiments with NEMO3.6 is available at https://github.com/ysilvy/simus_orca1_fluxforced. Simulation outputs can be made available upon request to Y.S. The python code created for the figures of this paper is available at https://doi.org/10.5281/zenodo.6606354.

APPENDIX

Nonlinear Additivity of the Ocean-Only Experiments

The nonlinear interactions between the different surface perturbations are presented in Fig. A1 by comparing the response to the all-forcing experiment to the sum of the responses to individual forcings. More specifically, we compare first BUOY to the sum of HEAT and WATER and then ALL to the sum of BUOY and STRESS, and again ALL to the sum of HEAT, WATER, and STRESS. Significant nonlinearities arise mainly in subpolar regions, where there are intense ventilation changes in the experiments and where the forced changes are large. In the subpolar North Atlantic, the nonadditivity is caused by nonlinear interactions between the two buoyancy flux perturbations (right panels in Fig. A1), while in the Southern Ocean nonlinearities are dominated by interactions between the buoyancy flux and the wind stress perturbations (middle panels), and to a smaller degree by interactions between the buoyancy flux perturbations themselves. These regions have also been identified as the most difficult to reproduce the exact same convection events in the CTL compared to the coupled piControl (not shown), as these are very sensitive mechanisms to the surface fluxes, and the 3-hourly forcing (twice the coupling frequency in the coupled model) is still insufficient for these types of events. We note that overall the evolution of the CTL temperature does not diverge in time from the piControl (Silvy et al. 2022) and validates the aims set for our scientific questions.

REFERENCES

Abrahamsen, E. P., and Coauthors, 2019: Stabilization of dense Antarctic water supply to the Atlantic Ocean overturning circulation. *Nat. Climate Change*, **9**, 742–746, https://doi.org/10.1038/s41558-019-0561-2.

Armour, K. C., J. Marshall, J. R. Scott, A. Donohoe, and E. R. Newsom, 2016: Southern Ocean warming delayed by circumpolar upwelling and equatorward transport. *Nat. Geosci.*, **9**, 549–554, https://doi.org/10.1038/ngeo2731.

Aumont, O., C. Ethé, A. Tagliabue, L. Bopp, and M. Gehlen, 2015: PISCES-v2: An ocean biogeochemical model for carbon and ecosystem studies. *Geosci. Model Dev.*, **8**, 2465–2513, https://doi.org/10.5194/gmd-8-2465-2015.

Banks, H. T., and J. M. Gregory, 2006: Mechanisms of ocean heat uptake in a coupled climate model and the implications for tracer based predictions of ocean heat uptake. *Geophys. Res. Lett.*, **33**, L07608, https://doi.org/10.1029/2005GL025352.

——, R. Wood, and J. Gregory, 2002: Changes to Indian Ocean Subantarctic Mode Water in a coupled climate model as CO_2 forcing increases. *J. Phys. Oceanogr.*, **32**, 12, https://doi.org/10.1175/1520-0485(2002)032<2816:CTIOSM>2.0.CO;2.

Bonnet, R., O. Boucher, J. Deshayes, G. Gastineau, F. Hourdin, J. Mignot, J. Servonnat, and D. Swingedouw, 2021a: Presentation and evaluation of the IPSL-CM6A-LR ensemble of

Brought to you by NOAA Central Library | Unauthenticated | Downloaded 01/23/24 09:28 PM UTC

extended historical simulations. *J. Adv. Model. Earth Syst.*, **25**, e2021MS002565, https://doi.org/10.1029/2021MS002565.

——, and Coauthors, 2021b: Increased risk of near term global warming due to a recent AMOC weakening. *Nat. Commun.*, **12**, 6108, https://doi.org/10.1038/s41467-021-26370-0.

Boucher, O., and Coauthors, 2020: Presentation and evaluation of the IPSL-CM6A-LR climate model. *J. Adv. Model. Earth Syst.*, **12**, e2019MS002010, https://doi.org/10.1029/2019MS002010.

Bronselaer, B., and L. Zanna, 2020: Heat and carbon coupling reveals ocean warming due to circulation changes. *Nature*, **584**, 227–233, https://doi.org/10.1038/s41586-020-2573-5.

——, M. Winton, S. M. Griffies, W. J. Hurlin, K. B. Rodgers, O. V. Sergienko, R. J. Stouffer, and J. L. Russell, 2018: Change in future climate due to Antarctic meltwater. *Nature*, **564**, 53–58, https://doi.org/10.1038/s41586-018-0712-z.

Couldrey, M. P., and Coauthors, 2021: What causes the spread of model projections of ocean dynamic sea-level change in response to greenhouse gas forcing? *Climate Dyn.*, **56**, 155–187, https://doi.org/10.1007/s00382-020-05471-4.

de Lavergne, C., J. B. Palter, E. D. Galbraith, R. Bernardello, and I. Marinov, 2014: Cessation of deep convection in the open Southern Ocean under anthropogenic climate change. *Nat. Climate Change*, **4**, 278–282, https://doi.org/10.1038/nclimate2132.

Deser, C., and Coauthors, 2020: Insights from Earth system model initial-condition large ensembles and future prospects. *Nat. Climate Change*, **10**, 277–286, https://doi.org/10.1038/s41558-020-0731-2.

DeVries, T., and F. Primeau, 2011: Dynamically and observationally constrained estimates of water-mass distributions and ages in the global ocean. *J. Phys. Oceanogr.*, **41**, 2381–2401, https://doi.org/10.1175/JPO-D-10-05011.1.

Dias, F. B., and Coauthors, 2020: Ocean heat storage in response to changing ocean circulation processes. *J. Climate*, **33**, 9065–9082, https://doi.org/10.1175/JCLI-D-19-1016.1.

——, and Coauthors, 2021: Subpolar Southern Ocean response to changes in the surface momentum, heat, and freshwater fluxes under 2×CO_2. *J. Climate*, **34**, 8755–8775, https://doi.org/10.1175/JCLI-D-21-0161.1.

Eyring, V., S. Bony, G. A. Meehl, C. A. Senior, B. Stevens, R. J. Stouffer, and K. E. Taylor, 2016: Overview of the Coupled Model Intercomparison Project Phase 6 (CMIP6) experimental design and organization. *Geosci. Model Dev.*, **9**, 1937–1958, https://doi.org/10.5194/gmd-9-1937-2016.

Fogwill, C. J., S. J. Phipps, C. S. M. Turney, and N. R. Golledge, 2015: Sensitivity of the Southern Ocean to enhanced regional Antarctic ice sheet meltwater input. *Earth's Future*, **3**, 317–329, https://doi.org/10.1002/2015EF000306.

Fox-Kemper, B., and Coauthors, 2021: Ocean, cryosphere and sea level change. *Climate Change 2021: The Physical Science Basis*, V. Masson-Delmotte et al., Eds., Cambridge University Press, 1211–1362, https://doi.org/10.1017/9781009157896.011.

Frölicher, T. L., J. L. Sarmiento, D. J. Paynter, J. P. Dunne, J. P. Krasting, and M. Winton, 2015: Dominance of the Southern Ocean in anthropogenic carbon and heat uptake in CMIP5 models. *J. Climate*, **28**, 862–886, https://doi.org/10.1175/JCLI-D-14-00117.1.

Fyfe, J. C., O. A. Saenko, K. Zickfeld, M. Eby, and A. J. Weaver, 2007: The role of poleward-intensifying winds on Southern Ocean warming. *J. Climate*, **20**, 5391–5400, https://doi.org/10.1175/2007JCLI1764.1.

Garuba, O. A., and B. A. Klinger, 2016: Ocean heat uptake and interbasin transport of the passive and redistributive components of surface heating. *J. Climate*, **29**, 7507–7527, https://doi.org/10.1175/JCLI-D-16-0138.1.

——, and ——, 2018: The role of individual surface flux components in the passive and active ocean heat uptake. *J. Climate*, **31**, 6157–6173, https://doi.org/10.1175/JCLI-D-17-0452.1.

Gidden, M. J., and Coauthors, 2019: Global emissions pathways under different socioeconomic scenarios for use in CMIP6: A dataset of harmonized emissions trajectories through the end of the century. *Geosci. Model Dev.*, **12**, 1443–1475, https://doi.org/10.5194/gmd-12-1443-2019.

Gregory, J. M., 2000: Vertical heat transports in the ocean and their effect on time-dependent climate change. *Climate Dyn.*, **16**, 501–515, https://doi.org/10.1007/s003820000059.

——, and Coauthors, 2016: The Flux-Anomaly-Forced Model Intercomparison Project (FAFMIP) contribution to CMIP6: Investigation of sea-level and ocean climate change in response to CO_2 forcing. *Geosci. Model Dev.*, **9**, 3993–4017, https://doi.org/10.5194/gmd-9-3993-2016.

Hanawa, K., and L. D. Talley, 2001: Modewaters. *Ocean Circulation and Climate*, G. Siedler, J. Church, and J. Gould, Eds., Academic Press, 373–386, https://doi.org/10.1016/S0074-6142(01)80129-7.

Hassan, T., R. J. Allen, W. Liu, and C. A. Randles, 2021: Anthropogenic aerosol forcing of the Atlantic meridional overturning circulation and the associated mechanisms in CMIP6 models. *Atmos. Chem. Phys.*, **21**, 5821–5846, https://doi.org/10.5194/acp-21-5821-2021.

Hawkins, E., and R. Sutton, 2012: Time of emergence of climate signals. *Geophys. Res. Lett.*, **39**, L01702, https://doi.org/10.1029/2011GL050087.

Heuzé, C., 2021: Antarctic Bottom Water and North Atlantic Deep Water in CMIP6 models. *Ocean Sci.*, **17**, 59–90, https://doi.org/10.5194/os-17-59-2021.

——, K. J. Heywood, D. P. Stevens, and J. K. Ridley, 2013: Southern Ocean bottom water characteristics in CMIP5 models. *Geophys. Res. Lett.*, **40**, 1409–1414, https://doi.org/10.1002/grl.50287.

——, M. Mohrmann, E. Andersson, and E. Crafoord, 2020: Global decline of deep water formation with increasing atmospheric CO_2. *Environ. Sci.*, https://doi.org/10.31223/X56K6D.

Hobbs, W. R., C. Roach, T. Roy, J.-B. Sallée, and N. Bindoff, 2021: Anthropogenic temperature and salinity changes in the Southern Ocean. *J. Climate*, **34**, 215–228, https://doi.org/10.1175/JCLI-D-20-0454.1.

Hourdin, F., and Coauthors, 2020: LMDZ6A: The atmospheric component of the IPSL climate model with improved and better tuned physics. *J. Adv. Model. Earth Syst.*, **12**, e2019MS001892, https://doi.org/10.1029/2019MS001892.

Hu, S., S.-P. Xie, and W. Liu, 2020: Global pattern formation of net ocean surface heat flux response to greenhouse warming. *J. Climate*, **33**, 7503–7522, https://doi.org/10.1175/JCLI-D-19-0642.1.

Huber, M. B., and L. Zanna, 2017: Drivers of uncertainty in simulated ocean circulation and heat uptake. *Geophys. Res. Lett.*, **44**, 1402–1413, https://doi.org/10.1002/2016GL071587.

IPCC, 2021: *Climate Change 2021: The Physical Science Basis.* V. Masson-Delmotte et al., Eds., Cambridge University Press, 3949 pp.

Jiang, W., G. Gastineau, and F. Codron, 2021: Multicentennial variability driven by salinity exchanges between the Atlantic and the Arctic Ocean in a coupled climate model. *J. Adv. Model. Earth Syst.*, **13**, e2020MS002366, https://doi.org/10.1029/2020MS002366.

Brought to you by NOAA Central Library | Unauthenticated | Downloaded 01/23/24 09:28 PM UTC

Johnson, G. C., 2008: Quantifying Antarctic Bottom Water and North Atlantic Deep Water volumes. *J. Geophys. Res.*, **113**, C05027, https://doi.org/10.1029/2007JC004477.

Krinner, G., and Coauthors, 2005: A dynamic global vegetation model for studies of the coupled atmosphere–biosphere system. *Global Biogeochem. Cycles*, **19**, GB1015, https://doi.org/10.1029/2003GB002199.

Lago, V., and M. H. England, 2019: Projected slowdown of Antarctic Bottom Water formation in response to amplified meltwater contributions. *J. Climate*, **32**, 6319–6335, https://doi.org/10.1175/JCLI-D-18-0622.1.

Liu, W., J. Lu, S.-P. Xie, and A. Fedorov, 2018: Southern Ocean heat uptake, redistribution, and storage in a warming climate: The role of meridional overturning circulation. *J. Climate*, **31**, 4727–4743, https://doi.org/10.1175/JCLI-D-17-0761.1.

Madec, G., and Coauthors, 2017: NEMO ocean engine. Zenodo, https://doi.org/10.5281/ZENODO.

Marshall, J., and K. Speer, 2012: Closure of the meridional overturning circulation through Southern Ocean upwelling. *Nat. Geosci.*, **5**, 171–180, https://doi.org/10.1038/ngeo1391.

——, J. R. Scott, K. C. Armour, J.-M. Campin, M. Kelley, and A. Romanou, 2015: The ocean's role in the transient response of climate to abrupt greenhouse gas forcing. *Climate Dyn.*, **44**, 2287–2299, https://doi.org/10.1007/s00382-014-2308-0.

Menary, M. B., and Coauthors, 2020: Aerosol-forced AMOC changes in CMIP6 historical simulations. *Geophys. Res. Lett.*, **47**, e2020GL088166, https://doi.org/10.1029/2020GL088166.

Mignot, J., and Coauthors, 2021: The tuning strategy of IPSL-CM6A-LR. *J. Adv. Model. Earth Syst.*, https://doi.org/10.1029/2020MS002340.

Mikolajewicz, U., and R. Voss, 2000: The role of the individual air–sea flux components in CO_2-induced changes of the ocean's circulation and climate. *Climate Dyn.*, **16**, 627–642, https://doi.org/10.1007/s003820000066.

Mohrmann, M., C. Heuzé, and S. Swart, 2021: Southern Ocean polynyas in CMIP6 models. *Cryosphere*, **15**, 4281–4313, https://doi.org/10.5194/tc-15-4281-2021.

Morrison, A. K., D. W. Waugh, A. M. Hogg, D. C. Jones, and R. P. Abernathey, 2022: Ventilation of the Southern Ocean pycnocline. *Annu. Rev. Mar. Sci.*, **14**, 405–430, https://doi.org/10.1146/annurev-marine-010419-011012.

Piecuch, C. G., R. M. Ponte, C. M. Little, M. W. Buckley, and I. Fukumori, 2017: Mechanisms underlying recent decadal changes in subpolar North Atlantic Ocean heat content. *J. Geophys. Res. Oceans*, **122**, 7181–7197, https://doi.org/10.1002/2017JC012845.

Rathore, S., N. L. Bindoff, H. E. Phillips, and M. Feng, 2020: Recent hemispheric asymmetry in global ocean warming induced by climate change and internal variability. *Nat. Commun.*, **11**, 2008, https://doi.org/10.1038/s41467-020-15754-3.

Roquet, F., G. Madec, T. J. McDougall, and P. M. Barker, 2015: Accurate polynomial expressions for the density and specific volume of seawater using the TEOS-10 standard. *Ocean Modell.*, **90**, 29–43, https://doi.org/10.1016/j.ocemod.2015.04.002.

Rousset, C., and Coauthors, 2015: The Louvain-La-Neuve sea ice model LIM3.6: Global and regional capabilities. *Geosci. Model Dev.*, **8**, 2991–3005, https://doi.org/10.5194/gmd-8-2991-2015.

Sallée, J.-B., E. Shuckburgh, N. Bruneau, A. J. S. Meijers, T. J. Bracegirdle, Z. Wang, and T. Roy, 2013: Assessment of Southern Ocean water mass circulation and characteristics in CMIP5 models: Historical bias and forcing response. *J. Geophys. Res. Oceans*, **118**, 1830–1844, https://doi.org/10.1002/jgrc.20135.

Sen Gupta, A. S., N. C. Jourdain, J. N. Brown, and D. Monselesan, 2013: Climate drift in the CMIP5 models. *J. Climate*, **26**, 8597–8615, https://doi.org/10.1175/JCLI-D-12-00521.1.

Shi, J.-R., S.-P. Xie, and L. D. Talley, 2018: Evolving relative importance of the Southern Ocean and North Atlantic in anthropogenic ocean heat uptake. *J. Climate*, **31**, 7459–7479, https://doi.org/10.1175/JCLI-D-18-0170.1.

——, L. D. Talley, S.-P. Xie, W. Liu, and S. T. Gille, 2020: Effects of buoyancy and wind forcing on southern ocean climate change. *J. Climate*, **33**, 10 003–10 020, https://doi.org/10.1175/JCLI-D-19-0877.1.

Silvano, A., S. R. Rintoul, B. Peña-Molino, and W. R. Hobbs, E. van Wijk, S. Aoki, T. Tamura, and G. D. Williams, 2018: Freshening by glacial meltwater enhances melting of ice shelves and reduces formation of Antarctic bottom water. *Sci. Adv.*, **4**, eaap9467, https://doi.org/10.1126/sciadv.aap9467.

——, and Coauthors, 2020: Recent recovery of Antarctic Bottom Water formation in the Ross Sea driven by climate anomalies. *Nat. Geosci.*, **13**, 780–786, https://doi.org/10.1038/s41561-020-00655-3.

Silvy, Y., 2022: Emergence of temperature and salinity changes in the ocean interior in response to climate change: Timescales and mechanisms. Ph.D. thesis, Sorbonne University, 245 pp., https://rgdoi.net/10.13140/RG.2.2.10983.93607.

——, E. Guilyardi, J.-B. Sallée, and P. J. Durack, 2020: Human-induced changes to the global ocean water masses and their time of emergence. *Nat. Climate Change*, **10**, 1030–1036, https://doi.org/10.1038/s41558-020-0878-x.

——, C. Rousset, E. Guilyardi, J.-B. Sallée, J. Mignot, C. Ethé, and G. Madec, 2022: A modeling framework to understand transient ocean climate change in large coupled ensembles. *Geosci. Model Dev.*, **15**, 7683–7713, https://doi.org/10.5194/gmd-15-7683-2022.

Swart, N. C., S. T. Gille, J. C. Fyfe, and N. P. Gillett, 2018: Recent Southern Ocean warming and freshening driven by greenhouse gas emissions and ozone depletion. *Nature Geosci.*, **11**, 836–841, https://doi.org/10.1038/s41561-018-0226-1.

Szopa, S., and Coauthors, 2021: Short-lived climate forcers. *Climate Change 2021: The Physical Science Basis*. Cambridge University Press, 817–922, doi:10.1017/9781009157896.008.

Talley, L. D., and M. E. Raymer, 1982: Eighteen degree water variability. *J. Mar. Res.*, **40**, 757–775, http://sam.ucsd.edu/ltalley/papers/1980s/talley_raymer_jmr_1982.pdf.

Todd, A., and Coauthors, 2020: Ocean-only FAFMIP: Understanding regional patterns of ocean heat content and dynamic sea level change. *J. Adv. Model. Earth Syst.*, **12**, https://doi.org/10.1029/2019MS002027.

Waugh, D. W., A. McC. Hogg, P. Spence, M. H. England, and T. W. N. Haine, 2019: Response of Southern Ocean ventilation to changes in midlatitude westerly winds. *J. Climate*, **32**, 5345–5361., https://doi.org/10.1175/JCLI-D-19-0039.1.

Williams, R. G., A. Katavouta, and V. Roussenov, 2021: Regional asymmetries in ocean heat and carbon storage due to dynamic redistribution in climate model projections. *J. Climate*, **34**, 3907–3925, https://doi.org/10.1175/JCLI-D-20-0519.1.

Winton, M., S. M. Griffies, B. L. Samuels, J. L. Sarmiento, and T. L. Frölicher, 2013: Connecting changing ocean circulation with changing climate. *J. Climate*, **26**, 2268–2278, https://doi.org/10.1175/JCLI-D-12-00296.1.

Brought to you by NOAA Central Library | Unauthenticated | Downloaded 01/23/24 09:28 PM UTC

Xie, P., and G. K. Vallis, 2012: The passive and active nature of ocean heat uptake in idealized climate change experiments. *Climate Dyn.*, **38**, 667–684, https://doi.org/10.1007/s00382-011-1063-8.

Zanna, L., J. M. Brankart, M. Huber, S. Leroux, T. Penduff, and P. D. Williams, 2019a: Uncertainty and scale interactions in ocean ensembles: From seasonal forecasts to multidecadal climate predictions. *Quart. J. Roy. Meteor. Soc.*, **145**, 160–175, https://doi.org/10.1002/qj.3397.

——, S. Khatiwala, J. M. Gregory, J. Ison, and P. Heimbach, 2019b: Global reconstruction of historical ocean heat storage and transport. *Proc. Natl. Acad. Sci. USA*, **116**, 1126–1131, https://doi.org/10.1073/pnas.1808838115.

Zika, J. D., J. M. Gregory, E. L. McDonagh, A. Marzocchi, and L. Clément, 2021: Recent water mass changes reveal mechanisms of ocean warming. *J. Climate*, **34**, 3461–3479, https://doi.org/10.1175/JCLI-D-20-0355.1.

Brought to you by NOAA Central Library | Unauthenticated | Downloaded 01/23/24 09:28 PM UTC